UNIVERSITY OF CALIFORNIA

Santa Barbara

Recycling of Continental Crust Captured in Pamir Xenoliths

A Thesis submitted in partial satisfaction of the

requirements for the degree Master of Science

in Earth Science

by

Madeline Ellen Faith Shaffer

Committee in charge:

Professor Bradley R. Hacker, Chair

Professor John M. Cottle

Professor Matthew G. Jackson

June 2017

The thesis of Madeline Ellen Faith Shaffer is approved.

_____

John Cottle

_____

Matthew Jackson

_____

Bradley Hacker, Committee Chair

May 2017

Recycling of Continental Crust Captured in Pamir Xenoliths

by

Madeline Ellen Faith Shaffer

ACKNOWLEDGEMENTS

I would foremost like to acknowledge my advisor, Brad, for his guidance and patience throughout the past two years. He has been integral in my growth from a student with a primarily archaeological background to a confident geologist. I initially met Brad through a Skype interview, where he described to me a one-of-a-kind opportunity to study unique crustal xenoliths from the Pamir. This thesis is the pinnacle of that study.

I also want to acknowledge the other students, faculty, and staff who have helped me develop ideas and collect data, and who also provided guidance throughout this process. Much of the following work was only possible with your support.

Finally, I would like to acknowledge my parents, who have always encouraged me to meet new opportunities and challenges with enthusiasm, and to my friends, who have provided a wealth of support and positivity during the past two years.

ABSTRACT

Recycling of Continental Crust Captured in Pamir Xenoliths

by

Madeline Ellen Faith Shaffer

Xenoliths that erupted in the SE Pamir of Tajikistan from 1000–1100°C and 90 km depth are exclusively crustal, providing a means of examining what happens to crust that founders into the mantle. $^{40}Ar/^{39}Ar$ dating of volcanic minerals indicates an eruption age of 10.0 ± 0.2 Ma. U-Pb + trace-element laser-ablation split stream inductively coupled plasma mass spectrometry of zircon shows that the xenoliths were likely derived from the crustal section into which they were intruded: the igneous xenoliths were derived from the Jurassic–Cretaceous Trans-Himalayan Batholith, and the metasedimentary xenoliths are like the stratigraphic section that hosts the Batholith. Recrystallization of these zircons was extensive, yielding a range of dates down to 10 Ma. The zircons show distinct changes in Eu anomaly, Lu/Gd ratio, and Ti concentrations compatible with garnet growth and minimal heating at 22−20 Ma, and then 200–300°C of heating, ~40 km of burial, and alkali−carbonate melt injection at 14−11 Ma. These dramatic changes are interpreted to coincide with foundering of the Pamir lower crust caused by tectonic thickening and northward rollback of the Asian slab. These xenoliths provide our only known record of the physical and chemical changes during the foundering continental crust.

TABLE OF CONTENTS

I. Introduction

Recycling of continental crust into the mantle is among the most-important processes driving the chemical and physical evolution of Earth. Mechanisms of crustal recycling include arc subduction, sediment subduction, continent subduction, subduction erosion, and foundering [e.g., *Hacker et al.*, 2015]. These processes dictate the rates and types of crustal chemical and physical evolution—and even more-fundamental issues such as the secular evolution of continental volume—but are only loosely understood. This limitation has led to a wide range of viewpoints on the efficiency of the recycling process. If, for example, 95% of continental crustal material that is ablated by subduction erosion is returned to the mantle—as suggested by *Scholl and von Huene* [2007]—this process may destroy continental crust as fast as it is produced [*Stern*, 2010], and the eroded material comes from all crustal levels. Alternatively, if crustal material carried into the mantle by subduction erosion undergoes buoyancy-driven fractionation, the mafic material may return to the mantle, and the felsic material may be relaminated to the base of the crust *[Hacker et al.*, 2011*; Hacker et al.*, 2015*; Kelemen and Behn,* 2016].

During the twilight of the geosyncline era and the dawn of the plate-tectonic revolution, *Ringwood and Green* [1966] realized that the basalt→eclogite transformation could drive crustal foundering, and Armstrong [1968] suggested that large-scale recycling of continental crust might occur by sediment subduction. Over the next few decades, crustal recycling via the foundering of gravitationally unstable lower portions of arcs [*Herzberg et al.*, 1983; *Arndt and Goldstein*, 1989; *Kay and Kay*, 1991], and via sediment subduction [*Hilde*, 1983] became mainstream concepts. The importance of crustal recycling by subduction erosion was recognized next [*Clift and Vannucchi*, 2004*;Scholl and von Huene*, 2007], and—once the

abundance of ultrahigh-pressure (UHP) terranes became clear [*Ernst*, 2001]—continental foundering and subduction [*Molnar and Gray*, 1979] were recognized as important recycling processes. The most-recent form of crustal recycling that has been suggested is arc subduction [*Tamura et al.*, 2010; *Hacker et al.*, 2011, 2015; *Kelemen & Behn*, 2016].

These crustal recycling processes are of supreme interest for understanding the evolution of Earth for many reasons:

- Selective removal of dense material changes the composition of Earth's crust, leading to secular variation in composition, or long-term chemical differentiation. Such changes have implications for the thickness, thermal structure, radioactivity profile, and velocity structure of the crust [*Herzberg et al.*, 1983; *Arndt and Goldstein*, 1989; *Kay and Kay*, 1991; *Jull and Kelemen*, 2001; *Behn and Kelemen*, 2006; *Kukkonen et al.*, 2008; *Hacker et al.*, 2011; *Lee*, 2014].
- Introduction of differentiated crust into the mantle produces local chemical heterogeneities in the mantle that may drive or affect melting, or enhance or diminish chemical buoyancy and thus gravity-driven motion [*Allègre and Turcotte*, 1986; *Arndt and Goldstein*, 1989; *Kay and Kay*, 1991; *Lee*, 2014].
- Continental crust is almost everywhere thinner than 50 km, suggesting that crust thicker than this is gravitationally unstable [*Anderson*, 2005] or weak [Sandiford, 2xxx].
- Changes in plate-scale forces resulting from the removal of dense material from the lithosphere can induce changes in plate motions [*Molnar et al.*, 1993].
- Intracontinental subduction may be an integral part of continental orogeny [*Burtman and Molnar*, 1993].

II. The Importance of Xenoliths

Our understanding of crustal recycling comes chiefly from i) geodynamic models [e.g., *Gerya and Meilick,* 2011], ii) large-scale box models that use isotopic systems to quantify recycling rates [*Coltice et al.*, 2000; *Simon and Lécuyer*, 2005]; iii) exposed arc rocks, from which one can infer the magnitude and timescale of lower crustal foundering [*Kelemen et al.*, 2003; *Ducea et al.*, 2013]; iv) geophysical images of foundering material [*Zandt and Carrigan*, 1993]; and v) xenoliths, which provide snapshots of processes at depth. Among these techniques, xenoliths provide our only actual samples of the materials and the physical and chemical processes involved in crustal recycling, and constitute our only way to verify or "ground truth" inferences made from geodynamic models, box models, exposed arcs, and geophysical images. For example, xenoliths provided the spectacular record of foundering of the Sierra Nevada arc lower crust and upper mantle [*Ducea and Saleeby*, 1996; *Chin et al.*, 2013], and the foundation for interpreting seismic wavespeeds as images of the recycling process [*Zandt and Carrigan*, 1993]. Despite the tremendous insight that xenoliths afford our understanding of crustal recycling, essentially all xenoliths from mantle depths are mafic or ultramafic, save two localities: one in the Pamir [*Lutkov*, 2003, 2005; Hacker et al., 2005] and one in Tibet [*Chan et al.*, 2009]. These unusual xenoliths thus present a unique opportunity to understand the chemical and physical processes that attend crustal recycling.

III. Geological Setting

The Pamir are the northwestern extent of Earth's largest, archetypal continent-collision zone, the Cenozoic India–Eurasia orogenic belt (**Fig. 1**). The collision zone has an extensive history [e.g. *Burtman and Molnar,* 1993*; Schwab et al.,* 2004*; Schmidt et al.,* 2011*;*

Robinson, 2015*; Kufner et al.*, 2016] that includes at least three postulated Cenozoic foundering events: two breakoffs of the subducting Indian slab [*Negredo et al.*, 2007*; Replumaz et al.*, 2010*; DeCelles et al.*, 2011], and one event involving foundering of the Asian slab [*Kufner et al.*, 2016] and/or lower crust [*Hacker et al.*, 2005*; Gordon et al.*, 2012*; Schmidt et al.*, 2011].

A few dozen meter- to decameter-scale diatremes, volcanic necks and shallow dikes pierce the surface of the southeastern Pamir Plateau. Known as the Dunkeldik suite, these volcanic rocks range from ultrapotassic tephrite to tephriphonolite [*Malz*, 2011], syenite and carbonatite, and locally carry abundant cm- to dm-sized xenoliths [*Dmitriev*, 1976; *Lutkov*, 2003; *Lutkov*, 2005]. The xenoliths are extremely unusual: they are crustal rocks metamorphosed at ultrahigh temperature (>1000°C) and mantle depth (90 km) [*Ducea et al.*, 2003; *Hacker et al*., 2005; *Gordon et al*., 2012]. Apart from a single occurrence of much smaller—but otherwise similar—xenoliths in southern Tibet [*Chan et al.*, 2009], these xenoliths are one-of-a-kind: no other continental-crust xenoliths from such high pressures and temperatures are known. They alone can tell us what happens during the recycling of continental crust.

These Pamir xenoliths are especially valuable for four reasons. 1) Unlike crustal rocks that were subducted to mantle depths and exhumed in ultrahigh-pressure metamorphic terrains, the xenoliths preserve fresh minerals and textures developed at extreme mantle conditions. 2) Because the xenoliths were erupted only 10 Myr ago [this study, *Ducea et al.*, 2003], geophysical investigations of the Pamir crust and mantle [*Mechie et al.*, 2012; *Schneider et al.*, 2013; *Sippl et al.*, 2013] help place the formation and eruption of the xenoliths in a geodynamic context not possible in older orogenic belts. 3) The xenoliths were erupted near

high-grade gneiss domes composed of the same rock types (**Fig. 1**) [*Gordon et al*., 2012], which evolved coevally with the xenoliths and were exhumed shortly after the xenoliths were erupted [*Schmidt et al.*, 2011; *Stübner et al.*, 2013b; Hacker et al., in press].These gneiss domes can be used as a reference for the type of crust from which the xenoliths might have been derived prior to foundering. 4) The xenoliths are large and contain large and abundant U- and Th-bearing accessory minerals that can be used to establish timing of events [*Ducea et al.*, 2003; *Kooijman et al.*, 2017].

Here we use zircon to quantify the chronology of P-T conditions experienced by the xenoliths *before and during this foundering event*. This study seeks to: i) define the P-T and metasomatic evolution of crustal xenoliths during a recycling event; ii) reconstruct the series of events that led to foundering via delamination beneath the Pamir; iii) estimate the size of the foundered material and its rate of foundering; and iv) discuss the implications for the late Cenozoic evolution of the Pamir.

IV. Xenolith Description

The Pamir xenolith suite used for this study includes 85 eclogite- and granulite-facies rocks ranging in composition from basalt to granodiorite to pelite, plus phlogopite–garnet pyroxenite and websterite [*Lutkov*, 2003; *Lutkov*, 2005]. Our sample collection consists of 29% mafic igneous rocks, 18% pelitic, 10% ultramafic, 41% intermediate-composition quartzofeldspathic rocks of igneous or sedimentary provenance, and 2 minettes. The volcanic host rock is strongly enriched in LILE (e.g., 7–8 wt% K_2O and La = 1000x chondrite) and depleted in HFSE (with arc-type Nb, Ta, and Ti anomalies) [*Malz*, 2011]. Its major- and trace-element compositions suggest low degrees of melting of phlogopite-bearing garnet

lherzolite at ~4 GPa (130 km depth) in the presence of ~10% "sediment" component [*Malz*, 2011].

Major-element thermobarometry, pseudosections, and oxygen-isotope thermometry indicate that the granulite-facies xenoliths reached temperatures of ~875–1000°C and pressures of ~1.8–2.3 GPa, and the eclogite-facies rocks reached ~1000–1100°C and ~2.5–2.8 GPa [*Hacker et al.*, 2005; *Gordon et al.*, 2012] (**Fig. 2**). These pressures equate to depths of 65–80 km and 85–95 km; the eclogite-facies rocks were certainly erupted from depths well below the present-day Moho (60–70 km; *Mechie et al.*, 2012], and the peak pressures suggest that the granulite-facies rocks likely were as well. The hottest xenoliths have textures indicating melt injection (represented now by crystallized K-feldspar + ternary carbonate), dehydration melting of biotite, and growth of eclogite-facies minerals in the presence of melt [*Hacker et al.*, 2005].

The quoted temperatures are quite high for crustal rocks and presumably reflect a combination of conductive heating and magma injection prior to eruption; they do not reflect heating during eruption because the length scales of elemental zoning in the minerals are incompatible with the short duration of the eruption (1–10 days) [*Hacker et al.*, 2005]. The pressures quoted for the eclogite-facies rocks were derived from net-transfer reactions with both positive and negative Clapeyron slopes and cannot be artifacts of inaccurate temperature determinations [*Hacker et al.*, 2005; *Gordon et al.*, 2012].

The first LA-ICP-MS dataset on the xenoliths [*Ducea et al.*, 2003]—constituting of 19 zircons analyzed in two thin sections—revealed that one xenolith is a Cretaceous igneous rock and a second was derived from Eocene sediment. These data require that the Pamir xenoliths were derived from Asian crust and *not* Indian crust, as the latter lacks Cretaceous

magmatic rocks. It is a strong argument against derivation of the xenoliths by subduction erosion because the leading edge of the upper plate (in Pakistan and India) is an accreted slice of *India* [*Hodges,* 2000; *Yin and Harrison,* 2000]. The xenoliths more likely reached mantle depths by foundering of Asian crust or intracontinental subduction of Asian crust [*Hacker et al.,* 2005; *Kufner et al.,* 2016]. Furthermore, *Gordon et al*. [2012] noted that most of the xenoliths are compositionally similar to the Pamir Barrovian domes, implying that the xenoliths may represent foundered Pamir lower crust [*Gordon et al.,* 2012].

The Pamir have widespread gneiss domes that expose high-grade Cenozoic rocks with bulk compositions and igneous, detrital, and metamorphic mineral dates similar to those of the xenoliths [*Robinson et al.,* 2004; *Robinson et al.,* 2007; *Schmidt et al.,* 2011; *Stearns et al.,* 2013; *Stübner et al.,* 2013a; *Stübner et al.,* 2013b; *Rutte et al.,* 2017a; *Rutte et al.,* 2017b]. The dome nearest the xenolith site, Shakhdara dome (**Fig. 1**), is dominated by Cretaceous plutonic rocks intruded into a Paleozoic clastic-dominated sedimentary section. Monazite, zircon, titanite, and garnet dates indicate that prograde metamorphism associated with crustal thickening in that dome began at 30 Ma and peaked around 16 Ma [*Schmidt et al.,* 2011; *Stearns et al.,* 2013; *Stübner et al.,* 2013b; *Hacker et al.,* in review]. The thickening (**Fig. 3**) led to the development of migmatitic gneisses (700–825°C and ~1.4–1.6 GPa; **Fig. 2**) [*Schmidt et al.,* 2011; *Hacker et al.,* in press] and may have contributed to a gravitationally unstable root. At 12 Ma—just prior to the xenoliths' eruption—exhumation of the gneiss domes began, reaching the surface by ~3 Ma (**Fig. 3.3**) [*Stübner et al.,* 2013a; *Stübner et al.,* 2013b]. The dome exhumation and the foundering of the Pamir xenoliths may have been coeval processes resulting from crustal thickening—with the base of the crust recycling into the mantle and partially erupted as xenoliths, and the middle−lower crust rising to the

surface. The P-T evolution of the xenoliths addresses the timing of these events, and reveals a coeval process of exhumation and foundering.

A. Petrography

The xenoliths contain mineral assemblages of garnet + alkali feldspar + quartz + rutile ± phlogopite (**Fig. 4A-C**) [*Lutkov,* 2003; *Lutkov et al.,* 2005; *Hacker et al.,* 2005; *Gordon et al.,* 2012]. Xenoliths with significant kyanite and/or quartz (and detrital zircon; see below) are inferred to be metasedimentary. Xenoliths with high clinopyroxene/feldspar ratios range from quartz monzonite to granodiorite to tonalite in composition; more-mafic rocks (that lack inherited zircon; see below) are most likely igneous, whereas the more-felsic quartzofeldspathic rocks (some of which have inherited zircon) may have igneous or sedimentary protoliths. Most of the minerals are interpreted to be refractory remains after extensive melt extraction, but phlogopite, K-feldspar, and ternary Fe-Mg-Ca carbonate in some rocks may have been magmatically injected prior to eruption (**Fig. 4D**).

The two minette xenoliths (DK28 and DK36) are porphyries, with phenocrysts of alkali-feldspar and high-Ti phlogopite set in a carbonate groundmass with accessory apatite and zircon (cf. *Rock, 1980;* **Fig. 4F**). DK28 contains one 500 μm garnet surrounded by a 50 μm corona of clinopyroxene (**Fig. 4E**) that may be a xenocryst.

V. Methods

Zircon from 30 eclogite-facies xenoliths was analyzed in thin section for U-Pb dates and REE-Ti concentrations to reconstruct the foundering process. Zircon was first located and labeled in thin section using back-scattered electron (BSE) imaging on an FEI Quanta 400f

scanning electron microscope. The zircons were then imaged with cathodoluminescence (CL) to reveal zoning and internal textures. Inclusions in zircon were investigated by BSE and energy-dispersive spectrometry on the FEI instrument; carbonate inclusions were subsequently analyzed by wavelength-dispersive spectrometry on a Cameca SX-100 electron-probe micro-analyzer. U-Pb dates and REE-Ti concentrations were measured using LASS (laser-ablation split-stream inductively coupled-plasma mass spectrometry) [*Kylander-Clark et al., 2013*]; the laser spots were 15 μm in diameter, the laser fluence was 100% of 3 mJ, and the laser repetition rate was 4 Hz. BSE + CL images were used to guide placement of the laser beam into specific zircon compositional zones to minimize mechanical mixing. Zircon 91500 [*Wiedenbeck et al.,* 1995] was used as the primary U-Pb reference material, and GJ1 zircon [*Jackson et al.,* 2004] was used as a secondary U-Pb reference material to assess accuracy. For elemental concentrations, GJ1 [*Liu et al.,* 2010] was employed as the primary reference material, and unknown elemental concentrations were normalized to a Zr concentration of 43.1 wt%. For quality control, the reference material 91500 was used as a secondary standard and yielded concentrations within 10% of published values. The raw U-Pb and trace-element data were reduced using Iolite version 2.5 [*Paton et al.,* 2011]. All analyses were conducted at the University of California, Santa Barbara.

A total of 1521 zircon spots were analyzed from 30 thin sections (**Table 1**). The data from each ablation spot were assessed with particular care to identify which data came from homogeneous zircon, and which did not. Data that i) show downhole zoning, ii) came from spots straddling more than one CL zone, iii) are strongly discordant, or iv) have low $^{206}Pb/^{204}Pb$ ratios were rejected from the dataset. The data were also screened to remove non-zircon analyses by removing those with unusual LREE or Ti abundances. The fewest data

were rejected from the non-pelite xenolith zircon cores, and the most were rejected from metasedimentary xenolith zircon cores, chiefly because the former are larger and less recrystallized. Conversely, relatively few data from the metasedimentary zircon rims were discarded compared to the non-pelite xenoliths. The final dataset consists of 1119 analyses.

Following *Rubatto* [2002], *Kelly and Harley* [2005], *Timms* [2011], and *Taylor et al*. [2015], pressure was determined qualitatively by observing changes in two aspects of zircon trace-element composition: i) Eu/Eu* related to plagioclase stability, and ii) HREE slope—expressed as a Lu/Gd ratio—related to garnet stability. The expectation is that foundering of the xenoliths caused i) plagioclase breakdown that released Eu that could be consumed by zircon, and ii) garnet growth that reduced the amount of HREE that could be incorporated in zircon.

Temperature was determined from zircon Ti concentration using the *Ferry and Watson* [2007] calibration with its approximate pressure dependence of 50°C/GPa; the *Hofmann et al*. [2014] calibration yields temperatures on average 43°C hotter. Temperatures were calculated for equilibration at both 1 GPa and 2 GPa. All the rocks contain the saturating phases quartz and rutile, and pseudosection calculations indicate that rutile was stable in most of the xenoliths at >1.2 GPa. Even if rutile was not present during the low-pressure evolution of the xenoliths, the reduced a_{TiO2} afforded by the presence of ilmenite [*Ghent and Stout*, 1984] or titanite [*Kapp et al.*, 2009] has a minor effect on temperature (<50°C).

$^{40}Ar/^{39}Ar$ dating was completed at Stanford University via stepwise degassing in a resistance furnace. The results were calculated using the decay-constant data and monitor ages of *Renne et al*. (2010).

VI. Results

A. $^{40}Ar/^{39}Ar$ geochronology

Phlogopite, leucite, and amphibole from the host volcanic rock, a porphyritic fergusite [*Dmitriev*, 1976], yielded a weighted mean $^{40}Ar/^{39}Ar$ date of 10.03 +0.23/-0.12 Ma, at 97.9% confidence. This is interpreted as the eruption age of the Dunkeldik ultrapotassic magmatic suite.

B. Zircon Zoning

Each thin section contains 5–60 zircons. The zircons are 50 to 200 μm in diameter, chiefly anhedral, and occur as matrix grains and inclusions—the latter hosted almost exclusively in garnet. They have different types of CL zoning, including oscillatory zoning, ghost zoning, flat-CL response, and metamict zones [*Corfu et al.,* 2003]. The zircons in the pelite xenoliths typically have small (5–15 μm diameter) cores with large (>25 μm wide) CL-flat rims (**Fig.5E–H**). Zircons in non-pelite xenoliths have large (40–100 μm diameter) oscillatory zoned cores with thin (micron-scale) flat-CL rims (**Fig. 5A–D**). In nearly all rocks, the oscillatory zoning in the zircon cores is variably replaced by irregularly shaped domains with either CL-flat (**Fig.5C**) or ghost zoning (**Fig.5D**); some of these replacement domains are preferentially developed along cracks or specific crystal sectors (**Fig.5C**). We interpret the oscillatory zoning to be igneous and the other types of zoning to be metamorphic—realizing that the "metamorphic" zoning was likely produced above the solidus in the presence of a mixed silicate–carbonatite fluid/melt [*Hacker et al.,* 2005]. Zircons from the minette xenoliths are large (~100 μm average) and have complex oscillatory zoning reminiscent of

kimberlitic zircon [*Corfu et al.,* 2003] (**Fig. 5I–L**). Sample DK25—an igneous sample—contains some zircon similar to that in the minettes.

C. U-Pb Zircon geochronology

The measured U-Pb isotopic ratios, uncorrected for common Pb, are summarized **Table 1** and **Figure 6**; the complete data suite is presented in **Supplemental Figure 1**. Data from matrix zircon are shown in black, and data from zircon included in other minerals (almost exclusively garnet) are red. Some data are concordant, and some are not. Some data are clearly discordant because of the presence of common Pb, whereas other data indicate the presence of inherited components (assuming the composition of common Pb is not unusual); the latter are green.

The concordant dates range from 159 ± 6 Ma to 10 Ma. The oldest concordant dates in a majority of samples are 159–107 Ma; almost universally, these Jurassic–Cretaceous dates come from zircon cores (**Fig.5**). Discordant isotopic ratios derived from zircon cores and indicative of inherited zircon are present in six samples; their upper intercept dates (projected from 10 Ma) range from 1691 Ma to 405 Ma. Additional similar zircon may be obscured by the presence of common Pb.

The Miocene dates come almost exclusively from zircon rims (the youngest date from a zircon included in garnet is 12 Ma). In the non-minette xenoliths, these dates are 15.8 ± 0.7 Ma to 10.6 ± 0.4 Ma, but in many of these samples—particularly those with large datasets—the Miocene dates form a slightly older cluster (shown as "mean dates" in **Figure 6** and **Supplement Figure 1**) of 14.9 Ma to 13.7 Ma

Minette xenolith zircon (as well as zircon with similar shapes and zoning from DK25) yield dates solely between 12 Ma and 10 Ma, with single populations yielding intercept dates of 10.9 ± 0.1 Ma to 10.4 ± 0.1 Ma (**Figure 7**).

D. Trace-element behavior

In the non-minette xenoliths, the zircon cores have REE abundances and patterns with strongly negative Eu/Eu* anomalies and positive HREE slopes (~100-10,000 times chondrite) typical of crustal, magmatic zircon [*Hoskin and Ireland*, 2000] (**Fig. 8**). In contrast, the zircon rims (with a few exceptions in **Figure 8A**) have reduced Eu/Eu* anomalies and flat HREE slopes that are typical of high-pressure metamorphic rocks recrystallized in the presence of garnet and absence of plagioclase [e.g., *Root et al.*, 2004; *Kylander-Clark et al.*, 2013]. The minette xenolith zircons are enriched in LREE relative to all the other zircons, and have HREE slopes that are intermediate between the cores and rims of the other xenoliths; xenolith DK25 has zircon cores with REE patterns like the non-minette zircons, and zircon rims with REE patterns similar to the minettes.

The differences in zircon trace-element patterns are correlated with U-Pb date (**Fig.9**). This was first reported by *Kooijman et al*. [2017], who used a small, preliminary dataset; the different conclusions presented here are based on ten-fold larger dataset. The two-orders-of-magnitude change from HREE-rich to HREE-depleted zircon corresponds with 22–20 Ma U-Pb dates (**Fig. 9A**). The change from a strongly negative Eu anomaly to a less-negative or positive Eu anomaly corresponds to zircon with 14 Ma U-Pb dates (**Fig. 9B**).

The Ti abundances, and Ti-in-zircon temperatures (**Fig. 9C,D**) of inclusion and matrix grains from all xenoliths also show distinct changes with respect to U-Pb date: i) zircon with

dates older than 20 Ma give temperatures of 800–850°C (depending on pressure); ii) zircon with 20–15 Ma dates may be 50°C hotter; zircon with 14–11 Ma dates yield temperatures up to 1150°C (including DK25 and the minettes).

E. Zircon inclusions

Seventy-six mineral inclusions in zircon from 12 samples were studied. The inclusions are 2–30 μm in diameter and typically in zircon cores. The inclusions in all rock types other than minette are dominantly ternary (Ca−Na−K) feldspar, alkali feldspar, and apatite. Igneous-protolith xenolith zircons also have minor quartz, biotite, hornblende, and ternary (Ca−Mg−Fe) carbonate inclusions; metasedimentary zircon also contain kyanite and ternary carbonate. Zircon in the two minette xenoliths and in DK25 contain phlogopite, alkali feldspar, apatite, and ternary carbonate. The ternary carbonates display micron-scale compositional zoning of Mg and Ca (**Fig. 10**), and are all included within Miocene zircon zones. They are compositionally identical in composition to the ternary carbonates reported by *Hacker et al.* [2005], which were interpreted to be derived from unmixing of a carbonate-rich alkalic melt [*Lee & Wyllie,* 1998]. That alkalic melt might have been derived by small degrees of melting of a mantle source metasomatized by unknown processes of unknown age, or it might have been derived by melting of a mechanical mixture of foundering Pamir crust (i.e., the xenoliths or like material) and mantle peridotite.

VII. Discussion

A. U-Pb & Trace-elements

Interpreting trace-element and U-Pb data for zircon at temperatures as high as those experienced by the Pamir xenoliths requires careful consideration. For example, to interpret the Ti concentration and the U-Pb date from a single spot within a zircon as a *T-t* datum requires that both developed at the same time and that neither has been reset. The Pamir zircons have radii of 20–50 μm and may have been held at a temperature of 800°C for 100 Myr. The characteristic lengthscale, L_{Ti} = SQRT(2*Dt*), for Ti diffusion in undamaged zircon for this temperatures and timescale is <<1 μm as determined from laboratory data [*Cherniak and Watson*, 2007], implying that the Ti-in-zircon temperatures were not affected by volume diffusion. The same is true for Pb, Yb, and Dy, for which laboratory diffusivities [*Cherniak et al.*, 1997; *Cherniak*, 2000] yield characteristic lengthscales smaller than the zircons in the Pamir xenoliths (**Fig. 11**).

A more serious concern is posed by the high temperatures experienced by the xenoliths in the few million years prior to eruption. The U-Pb–Ti data in **Figure 8** imply that the Pamir zircons experienced temperatures up to 1100°C for 1–4 Myr. These high temperatures are in accord with those inferred for the hottest xenoliths from garnet, clinopyroxene, and feldspar compositions [*Hacker et al.*, 2005], meaning that they are not simply the result of 1100°C zircon crystallizing during melt infiltration. The characteristic lengthscale for Ti diffusion at 1000–1100°C and 1–4 Myr is still very small compared to zircon size (**Fig. 11**), implying, again, that the Ti-in-zircon temperatures were not affected by volume diffusion—and therefore are accurate representations of temperatures experienced by the xenoliths. Not so for Pb and Yb, however, which have laboratory diffusivities at these temperatures ~3 orders of magnitude faster than Ti, and, consequently, much longer diffusive lengthscales (**Fig. 11**). If the temperature reached 1000–1100°C for 1–4 Myr, the laboratory data indicate L_{Pb} = 20–

250 μm, L_{Dy} = 5–115 μm and L_{Yb} = 15–300 μm, enough to strongly modify U-Pb dates, Dy, and Lu/Dy ratios in zircon cores.

The zircon CL zoning and U-Pb date spot distributions lend additional insight to the question of how to interpret the trace-element + U-Pb data. 1) Some zircons have well-preserved, submicron-scale zoning visible in CL, and the CL-visible boundaries between the older core domains and the younger, Miocene rims are locally sharp. Dy is the main CL-active element in zircon [*Mariano*, 1989], and L_{Dy} is 5–115 μm for 1000–1100°C and 1–4 Myr (**Fig. 11**), implying that volume diffusion of Dy should have erased fine-scale CL zoning. 2) Some zircons have old U-Pb core dates and young rim dates, and others have young U-Pb core dates and old rim dates (e.g., **Fig. 5d**). Moreover, there is no simple relationship between U-Pb date and laser spot position within a grain (**Fig. 12**). Both of these observations are counter to the expected results of volume diffusion of Pb, particularly if L_{Pb} is 20–250 μm for 1000–1100°C and 1–4 Myr. Thus, the preservation of CL zoning and the heterogeneous preservation of U-Pb dates indicates that either the laboratory data describing volume diffusion do not apply to these zircons [*Kramers et al*., 2009], or the duration of heating was << 1 Myr (**Fig. 11**).

The CL zoning and U-Pb date distributions in **Figure 5** make it clear that—although volume diffusion of Pb may not have been important—some other mechanism caused Pb and Dy mobility in many grains. The mechanism that permitted this in situ zircon recrystallization is unknown, but may have involved corrosive mixed silicate–carbonate fluid that invaded portions of zircon that were cracked, contained more crystal defects, or were subject to higher deviatoric stress; all of these are possible in a rock undergoing the type of extreme metamorphism experienced by these xenoliths. Textural evidence of *in situ*

recrystallization is more pronounced in the metasedimentary xenoliths, and may be related to the colder solidi typical of such rocks.

A few zircon included in garnet are older than matrix zircon in the same rock (e.g., DK1 and DK33), indicating that garnet may have effectively shielded the zircon from recrystallization. In general, however, matrix zircon and included zircon do not have different dates, indicating that garnet typically was not an effective shield of zircon. Alternatively, some of the garnet may have grown after the youngest zircon inclusions—i.e., as late as 13 Ma. This last possibility is supported by the presence of major-element zoning in garnet and by the preservation of carbonate with fine-scale zoning in some garnet cores (Fig. 2k in *Hacker et al.* [2005]).

Thus, our interpretation is that the youngest dates in each sample represent the last time zircon either grew *de novo* or underwent *in situ* recrystallization; the most-common time for this was 14–11 Ma. The Jurassic–Cretaceous, 159–107 Ma, dates in a majority of samples are similar to the Cretaceous batholith exposed in the southern Pamir [*Schwab et al.,* 2004; *Stearns et al.,* 2013]; these may be viewed as minimum igneous crystallization ages. Upper intercept dates in the 1691 Ma to 405 Ma range in some samples are best interpreted as minimum ages of inherited grains; these dates are similar to the dates of zircons reported elsewhere in the Pamir [*Schwab et al.,* 2004; *Rutte et al*., 2017b]. In each sample, all the dates that are younger than the oldest concordant date and older than Miocene are very likely geologically meaningless dates that resulted from fine-scale, heterogeneous recrystallization in the Miocene. The interpretation that one xenolith was derived from Eocene sedimentary rocks [*Ducea et al.,* 2003] is wrong, as is the conclusion that there was punctuated zircon recrystallization [*Kooijman et al.,* 2017].

When in the Miocene did this partial recrystallization occur? The clusters of 14.9 Ma to 13.7 Ma zircon dates in the most-analyzed samples might provide an older boundary because they are not skewed toward younger dates. The 10.9 ± 0.1 Ma to 10.4 ± 0.1 Ma dates for the minette and DK25 zircons must be a younger bound. Thus, the Miocene partial recrystallization was likely ~14 Ma to 11 Ma.

The heterogeneous zircon recrystallization means that the time-dependent relationships exhibited by Lu/Gd, Eu/Eu*, and Ti-in-zircon must be carefully evaluated. Simplest to consider is Ti: volume diffusion of Ti is unlikely to have occurred, and yet the U-Pb dates could have been variably reset to younger dates by Pb mobility (**Fig. 11**). The 800°C Ti-in-zircon temperature of all the >14 Ma dates may simply represent igneous crystallization conditions during the Jurassic–Cretaceous or even earlier. The abruptness of the 14 Ma Ti increase (**Fig. 9C,D**) makes Pb resetting of ≤ 14 Ma data less probable, and is compatible with the Ti increase actually occurring at 14 Ma. The same logic applies to the marked drop in Lu/Gd ratio at 22–20 Ma and the marked increase in Eu/Eu* at 14–11 Ma.

By combining the T-t record of **Figure 9** with the P-T path of **Figure 2**, we reconstruct the P-T-t path of the Pamir xenoliths in **Figure 13**. From **Figure 9**, we take the Ti-in-zircon concentration to have been 5–10 ppm at ≥15 Ma, 50–80 ppm at 14 Ma, and 80–90 ppm at 11 Ma. The implication is that the xenoliths were heated ~200°C between 15 Ma and 14 Ma, and then sank ~20 km downward from 14 Ma until eruption at 10 Ma. The two-orders-of-magnitude change from HREE-rich to HREE-depleted zircon that corresponds with 22–20 Ma U-Pb dates may reflect thermally driven garnet growth; this coincides exactly in time with the 21–19 Ma dates for peak-pressure metamorphism in the Shakhdara dome (Fig 13; *Hacker et al*., in press). The change in Eu anomaly at 14 Ma—if it reflects the breakdown of

plagioclase (gray boundary in **Fig. 13**)—coincides with the 30–40 km increase in depth at 14–11 Ma inferred from P-T and Ti-in-zircon data.

B. Metasomatism/Magmatism

Nearly all the xenoliths show evidence of metasomatism by an ultrapotassic + carbonatitic melt. The uncommonly high mode of alkali feldspar and phlogopite is suggestive of K addition, particularly in the mafic rocks. At least one xenolith contains euhedral garnet and clinopyroxene projecting into K-feldspar—compatible with growth into a potassic melt (Figure 2L in *Hacker et al*. [2005]). Some xenoliths also contain carbonate as a matrix phase (e.g., Figure 2C in *Hacker et al*. [2005]) or as an inclusion in garnet and zircon. Numerous zircons contain additional inclusions of alkali feldspar and high-Ti biotite. These zircon inclusion types are in 14–11 Ma zircon, compatible with alkaline magma injection at that time.

The two minettes, DK28 and DK36, may be direct samples of this melt. We calculated the bulk composition of DK36 from point-counted mineral modes and mineral compositions measured by electron microprobe (**Table 2**); the rock is more potassic than any of the ultrapotassic volcanic rocks in the Dunkeldik suite studied by *Malz* [2011]. In fact, it is so potassic that it may be a partial cumulate. Minettes are calc-alkaline lamprophyres that commonly include porphyritic phlogopite and a sanidine + carbonate groundmass [*Le Maître*, 2002]. They originate from partial melting of peridotite that interacted with crust, and are commonly associated with carbonatite [*Rock, 1980; Rock, 1984; Niu et al., 2017*]. Whether the Asian mantle from which the Pamir minettes were derived inherited its crustal signature from crustal assimilation remains unresolved, but the occurrence of a garnet xenocryst in

DK28 is compatible with the former, as are the biotite breakdown textures in Figure 2A and 2B of *Hacker et al*. [2005] indicating that melting of the Pamir xenoliths was generating potassic melt.

The textures and trace-element abundances of zircon in xenolith DK25 provide strong support for the interpretation of the minettes as eruption-related magmatic rocks. DK25 has a mineral assemblage similar to the igneous xenoliths, and contains zircon with Cretaceous cores overgrown by Miocene rims, just like most of the other xenoliths. Additionally, some zircons in DK25 resemble the peculiar textures and REE-behavior of the minette xenoliths: they exhibit skeletal and convoluted zones, and are enriched in LREEs with a relatively flat HREE slope. Furthermore, the inclusions in DK25 zircon include ternary carbonate, high-Ti biotite, and alkali feldspar (particularly within zircon zones that have minette-style REEs).

C. Tectonic Implications

The xenoliths imply a Cenozoic evolution of the Pamir that matches several tectonic models. Cenozoic contractional deformation of the Pamir crust is inferred to have been driven by viscous coupling with the northward underthrusting Indian slab [*Stübner et al.,* 2013; *Sippl et al.,* 2013b; *Stearns et al.,* 2015; *Kufner et al.,* 2016; *Rutte et al.,* 2017]. Breakoff of that slab at ~25–20 Ma is presumed to have initiated large-scale extension within the Pamir crust. Afterward, when Indian mantle lithosphere resumed northward underthrusting of Asia at ~20 Ma, re-coupling of the slab with the Pamir crust is inferred to have driven additional N-S shortening, causing the rheologically weak Pamir crust to thicken dramatically and induce rollback of the Asian slab [*Schneider et al.,* 2013; *Sippl et al.,* 2013a, 2013b]. Garnet growth in the xenoliths at 22−20 Ma coincides with the time of this contraction. Sometime thereafter, the critically thickened Pamir crust became gravitationally

unstable and began to founder. The >200°C heating recorded in the xenoliths at ~14 Ma is likely to have taken place while the foundering was in progress. In terms of the size of foundered material, if we assume that the xenoliths were all derived from a single foundering sphere of crust that was heated solely by conduction, we can estimate the length scale of the sphere from the observation that heating from 800°C to >1000°C required ~1 Myr (15–14 Ma). The approximation x=2*SQRT(Kt), and a thermal diffusivity $\boldsymbol{K} = 10^{-6}$ m^2/s, yields a radius of ~10 km.

If the pre-Cenozoic Pamir crust was only 35–40 km thick, the accommodation of 900 km of Cenozoic convergence not only produced the present 70-km thick crust, but also led to another 40 km of 'excess' crust that was either extruded laterally or recycled into the mantle [*Schmidt et al.*, 2011]. The Pamir xenoliths may be just the tiniest glimpse of vast amounts of crustal recycling in the western India−Asia collision zone.

VIII. Conclusions

Miocene granulite- and eclogite-facies xenoliths from the Pamir of Tajikistan provide a unique and spectacular record of foundering of continental crust to mantle depths of 90 km. Coupled U-Pb dates and trace-element abundances measured by laser-ablation split stream inductively coupled plasma mass spectrometry reveal the evolution of the xenoliths. The xenoliths were derived from mixed sedimentary−igneous crust like that exposed today in gneiss domes nearby. At 22−20 Ma, the xenoliths passed into the garnet stability field with minimal heating. At 14−11 Ma, the xenoliths were heated 200−300°C, buried to depths of 90 km depth—20−40 km below the present Moho—and invaded by ultrapotassic/carbonatitic melt. At 10 Ma the xenoliths were erupted. The 14−10 Ma evolution is interpreted as the

response to foundering of a ~20 km wavelength instability of the Pamir lower crust created by large-scale Cenozoic crustal thickening and northward rollback of the Asian mantle from beneath the Pamir.

References

Allègre, C. J., and D. L. Turcotte (1986), Implications of a two-component marble-cake mantle, *Nature*, *323*, 123-127.

Anderson, D. H. (2005), Large Igneous Provinces, Delamination, and Fertile Mantle, *Elements*, *1*, 271-275.

Armstrong, R. A. (1968), A Model fo the evolution of strontium and lead isotopes in a dynamic Earth, *Reviews of Geophysics*, *6*, 175-199.

Arndt, N. T., and S. L. Goldstein (1989), An open boundary between lower continental crust and mantle; its role in crust formation and crustal recycling, *Tectonophysics*, *161*(3-4), 201-212.

Behn, M. D., and P. B. Kelemen (2006), The stability of arc lower crust: Insights from the Talkeetna arc section, south-central Alaska and the seismic structure of modern arcs, *Journal of Geophysical Research*, *111*, B11207, doi:11210.11029/12006JB004327.

Burtman, V. S., and P. Molnar (1993), Geological and geophysical evidence for deep subduction of continental crust beneath the Pamir, *Geological Society of America Special Paper*, *281*, 1-76.

Chan, G. H.-N., D. J. Waters, M. P. Searle, J. C. Aitchison, M. S. A. Horstwood, Q. Crowley, C.-H. Lo, and J. S.-L. Chan (2009), Probing the basement of southern Tibet: evidence from crustal xenoliths entrained in a Miocene ultrapotassic dyke, *Journal of the Geological Society, London*, *166*, 45-52. doi: 10.1144/0016-76492007-76492145.

Cherniak, D. J. (2000), Pb diffusion in zircon, *Chemical Geology*, *172*, 5-24.

Cherniak, D. J., and E. B. Watson (2007), Ti diffusion in zircon, *Chemical Geology*, *242*, 470-483.

Cherniak, D. J., J. M. Hanchar, and E. B. Watson (1997), Rare-earth diffusion in zircon, *Chemical Geology*, *134*, 289-301.

Chin, E. J., C. T. A. Lee, D. L. Tollstrup, L. Xie, J. B. Wimpenny, and Q. Z. Yin (2013), On the origin of hot metasedimentary quartzites in the lower crust of continental arcs, *Earth and Planetary Science Letters*, *361*, 120-133.

Clift, P., and P. Vannucchi (2004), Controls on tectonic accretion versus erosion in subduction zones: Implications for the origin and recycling of the continental crust, *Reviews of Geophysics*, *42*, doi:10.1029/2003RG000127.

Coltice, N., F. Albarede, and P. Gillet (2000), 40K-40Ar constraints on recycling continental crust into the mantle, *Science*, *288*, 845-847.

Corfu, F., Hanchar, J. M., Hoskin, P. W., & Kinny, P. (2003), Atlas of zircon textures, *Reviews in mineralogy and geochemistry*, *53*(1), 469-500.

DeCelles, P. G., Kapp, P., Quade, J., & Gehrels, G. E. (2011), Oligocene–Miocene Kailas basin, southwestern Tibet: Record of postcollisional upper-plate extension in the Indus-Yarlung suture zone, *Geological Society of America Bulletin*, *123*(7-8), 1337-1362.

Ducea, M. N., and J. B. Saleeby (1996), Buoyancy sources for a large unrooted mountain range, the Sierra Nevada, California: Evidence from xenolith thermobarometry, *Journal of Geophysical Research*, *101*, 8229-8241.

Ducea, M. N., A. C. Seclaman, K. E. Murray, D. Jianu, and L. M. Schoenbohm (2013), Mantle-drip magmatism beneath the Altiplano-Puna plateau, central Andes, *Geology*, *41*, 915-918.

Ducea, M. N., V. Lutkov, V. T. Minaev, B. Hacker, L. Ratschbacher, P. Luffi, M. Schwab, G. E. Gehrels, M. McWilliams, J. Vervoort, and J. Metcalf (2003), Building the Pamirs: the view from the underside, *Geology*, *31*, 849–852.

Ernst, W. G. (2001), Subduction, ultrahigh-pressure metamorphism, and regurgitation of buoyant crustal slices – implications for arcs and continental growth, *Physics of the Earth and Planetary Interiors*, *127*, 253-275.

Gerya, T. V., and F. I. Meilick (2011), Geodynamic regimes of subduction under an active margin: effects of rheological weakening by fluids and melts, *Journal of Metamorphic Geology*, *29*, 7-31.

Ghent, E. D., and M. Z. Stout (1984), TiO2 activity in metamorphosed pelitic and basic rocks: principles and applications to metamorphism in southeastern Canadian Cordillera, *Contributions to Mineralogy and Petrology*, *86*, 248–255.

Gordon, S. M., P. I. Luffi, B. R. Hacker, J. W. Valley, M. Spicuzza, R. Kozdon, P. Kelemen, L. Ratschbacher, and V. Minaev (2012), The thermal structure of continental crust in active orogens: Insight from Miocene eclogite- and granulite-facies xenoliths of the Pamir, *Journal of Metamorphic Geology*, *20*, 413–434.

Hacker, B. R., P. B. Kelemen, and M. D. Behn (2011), Differentiation of the continental crust by relamination, *Earth and Planetary Science Letters*, *307*, 501-516.

Hacker, B. R., Ritzwoller, M. H., & Xie, J. (2014), Partially melted, mica-bearing crust in Central Tibet, *Tectonics*, *33*(7), 1408-1424.

Hacker, B. R., P. Kelemen, and M. D. Behn (2015), Continental Lower Crust, *Annual Review of Earth and Planetary Sciences*.

Hacker, B. R., L. Ratschbacher, D. Rutte, M. A. Stearns, N. Malz, K. Stübner, A. R. C. Kylander-Clark, J. Pfänder, and A. Everson (in review), Building the Pamir-Tibet Plateau-Crustal stacking, extensional collapse, and lateral extrusion in the Central Pamir: 3. Thermobarometry and Petrochronology of Deep Asian Crust, *Tectonics*.

Hacker, B. R., P. Luffi, V. Lutkov, V. Minaev, L. Ratschbacher, T. Plank, M. Ducea, A. Patiño-Douce, M. McWilliams, and J. Metcalf (2005), Near-ultrahigh pressure processing of continental crust: Miocene crustal xenoliths from the Pamir, *Journal of Petrology*, *46*, 1661-1687.

Herzberg, C. T., W. S. Fyfe, and M. J. Carr (1983), Density constraints on the formation of the continental Moho and crust, *Contributions to Mineralogy and Petrology*, *84*(1), 1-5.

Hilde, T. W. C. (1983), Sediment subduction versus accretion around the Pacific, *Tectonophysics*, *99*, 381-397.

Hodges, K. V. (2000), Tectonics of the Himalaya and southern Tibet from two perspectives, *Geological Society of America Bulletin*, *112*, 324-350.

Jackson, S. E., Pearson, N. J., Griffin, W. L., & Belousova, E. A. (2004), The application of laser ablation-inductively coupled plasma-mass spectrometry to in situ U–Pb zircon geochronology, *Chemical Geology*, *211*(1), 47-69.

Jull, M., and P. B. Kelemen (2001), On the conditions for lower crustal convective instability, *Journal of Geophysical Research*, *106*, 6423–6445.

Kapp, P., C. E. Manning, and P. Tropper (2009), Phase-equilibrium constraints on titanite and rutile activities in mafic epidote amphibolites and geobarometry using titanite-rutile equilibria, *Journal of Metamorphic Geology*, *27*(7), 509-521.

Kay, R. W., and S. M. Kay (1991), Creation and destruction of lower continental crust, *Geologische Rundschau*, *80*, 259-278.

Kelemen, P., and M. D. Behn (2016), Formation of lower continental crust by relamination of buoyant arc lavas and plutons, *Nature Geoscience*, *DOI: 10.1038/NGEO2662*.

Kelemen, P. B., K. Hanghøj, and A. Greene (2003), One view of the geochemistry of subduction-related magmatic arcs, with an emphasis on primitive andesite and lower crust, in *The Crust, Vol. 3, Treatise on Geochemistry, (H.D. Holland and K.K. Turekian, eds.)*, edited by R. L. Rudnick, pp. 593-659, Elsevier-Pergamon, Oxford.

Kelly, N. M., and S. L. Harley (2005), An integrated microtextural and chemical approach to zircon geochronology: refining the Archaean history of the Napier Complex, east Antarctica, *Contributions to Mineral and Petrology*, *149*, 57-84.

Kramers, J., R. Frei, M. Newville, B. Kober, and I. Villa (2009), On the valency state of radiogenic lead in zircon and its consequences, Chemical Geology, 261, 4-11.

Kretz, R. (1983), Symbols for rock-forming minerals, *American Mineralogist*, *68*, 277–279.

Kukkonen, I. T., M. Kuusisto, M. Lehtonen, and P. Peltonen (2008), Delamination of eclogitized lower crust: Control on the crust-mantle boundary in the central Fennoscandian shield, *Tectonophysics*, *457*, 111-127.

Kufner, S. K., Schurr, B., Sippl, C., Yuan, X., Ratschbacher, L., Ischuk, A., et al. (2016), Deep India meets deep Asia: Lithospheric indentation, delamination and break-off under Pamir and Hindu Kush (Central Asia), *Earth and Planetary Science Letters*, *435*, 171-184.

Kylander-Clark, A. R., Hacker, B. R., & Cottle, J. M. (2013), Laser-ablation split-stream ICP petrochronology, *Chemical Geology*, *345*, 99-112.

Le Maitre, R. W., Streckeisen, A., Zanettin, B., Le Bas, M. J., Bonin, B., Bateman, P., et al. (2002), Igneous rocks: A classification and glossary of terms; Recommendations of the International Union of Geological Sciences, In *Subcommission on the Systematics of Igneous rocks*. Cambridge University Press.

Lee, C. T. A. (2014), Physics and chemistry of continental crust recycling, *Treatise on Geochemistry*.

Lutkov, V. S. (2003), Petrochemical evolution and genesis of potassium pyroxenite-eclogite-granulite association in the mantle and crustal xenoliths from Neogene fergusites of South Pamir, Tajikistan, *Geochimia*, *3*, 254-265.

Malz, N. (2011), Trace-element and isotopic composition of magmatic rocks from the Pamirs-petrogenetic and geodynamic implications, 73 pp, Freiberg Universität, Freiberg.

Mariano, A. N. (1989), Cathodoluminescence emission spectra of rare earth element activators in minerals, *Reviews in Mineralogy*, *21*, 339-348.

Mechie, J., X. Yuan, B. Schurr, F. Schneider, C. Sippl, L. Ratschbacher, V. Minaev, M. Gadoev, I. Oimahmadov, U. Abdybachaev, B. Moldobekov, S. Orunbaev, and S. Negmatullaev (2012), Crustal and uppermost mantle velocity structure along a profile across the Pamir and southern Tien Shan as derived from project TIPAGE wide-angle seismic data, *Geophysical Journal International*, *188*, 385-407.

Molnar, P., and D. Gray (1979), Subduction of continental lithosphere: some constraints and uncertainties, *Geology*, *7*, 58-62.

Molnar, P., P. England, and J. Martinod (1993), Mantle dynamics, uplift of the Tibetan Plateau and the Indian Monsoon, *Reviews of Geophysics*, *31*, 357-396.

Negredo, A. M., Replumaz, A., Villaseñor, A., & Guillot, S. (2007), Modeling the evolution of continental subduction processes in the Pamir–Hindu Kush region, *Earth and Planetary Science Letters*, *259*(1), 212-225.

Niu, X., Chen, B., Feng, G., Liu, F., & Yang, J. (2017), Origin of lamprophyres from the northern margin of the North China Craton: implications for mantle metasomatism, *Journal of the Geological Society*, *174*(2), 353-364.

Paton, C., Hellstrom, J., Paul, B., Woodhead, J., & Hergt, J. (2011), Iolite: Freeware for the visualisation and processing of mass spectrometric data, *Journal of Analytical Atomic Spectrometry*, *26*(12), 2508-2518.

Renne, P. R., Mundil, R., Balco, G., Min, K., & Ludwig, K. R. (2010), Joint determination of 40 K decay constants and 40 Ar∗/40 K for the Fish Canyon sanidine standard, and improved accuracy for 40 Ar/39 Ar geochronology, *Geochimica et Cosmochimica Acta*, *74*(18), 5349-5367.

Replumaz, A., Negredo, A. M., Guillot, S., & Villaseñor, A. (2010), Multiple episodes of continental subduction during India/Asia convergence: Insight from seismic tomography and tectonic reconstruction, *Tectonophysics*, *483*(1), 125-134.

Ringwood, A. E., and D. H. Green (1966), An experimental investigation of the gabbro-eclogite transformation and some geophysical implications, *Tectonophysics*, *3*, 383–427.

Robinson, A. C., A. Yin, C. E. Manning, T. M. Harrison, S. Zhang, and X. Wang (2004), Tectonic evolution of the northeastern Pamir; constraints from the northern portion of the Cenozoic Kongur Shan extensional system, western China, *Geological Society of America Bulletin*, *116*, 953-973.

Robinson, A. C., A. Yin, C. E. Manning, T. M. Harrison, S.-H. Zhang, and X.-F. Wang (2007), Cenozoic evolution of the eastern Pamir: Implications for strain-accommodation mechanisms at the western end of the Himalayan-Tibetan orogen, *Geological Society of America Bulletin*, *119*, 882-896.

Rock, N. M. (1980), "Rare-earth and other trace element contents and the origin of minettes." A critical comment on a paper by Bachinski and Scott (1979), *Geochimica et Cosmochimica Acta*, *44*(9), 1385-1388.

Rock, N. M. S. (1984), Nature and origin of calc-alkaline lamprophyres: minettes, vogesites, kersantites and spessartites, *Transactions of the Royal Society of Edinburgh: Earth Sciences*, *74*(04), 193-227.

Rubatto, D. (2002), Zircon trace element geochemistry: partitioning with garnet and the link between U-Pb ages and metamorphism, *Chemical Geology*, *184*, 123-138.

Rutte, D., Lothar, R., Schneider, S., Stübner, K., Stearns, M. A., Gulzar, M. A., & Hacker, B. R. (2017), Building the Pamir-Tibet Plateau—Crustal Stacking, Extensional Collapse, and Lateral Extrusion in the Central Pamir: 1. Geometry and Kinematics, *Tectonics*.

Rutte, D., Ratschbacher, L., Khan, J., Stübner, K., Hacker, B. R., Stearns, M. A., et al. (2017), Building the Pamir-Tibet Plateau—Crustal stacking, Extensional Collapse, and Lateral Extrusion in the Central Pamir: 2. Timing and Rates, *Tectonics*.

Schmidt, J., B. R. Hacker, L. Ratschbacher, K. Stübner, M. A. Stearns, A. Kylander-Clark, J. M. Cottle, A. A. G. Webb, G. Gehrels, and V. Minaev (2011), Cenozoic deep crust in the Pamir, *Earth and Planetary Science Letters*, *312*, 411-421.

Schneider, F. M., X. Yuan, B. Schurr, J. Mechie, C. Sippl, C. Haberland, V. Minaev, I. Oimahmadov, M. Gadoev, N. Radjabov, U. Abdybachaev, S. Orunbaev, and S. Negmatullaev (2013), Seismic imaging of subducting continental lower crust beneath the Pamir, *Earth and Planetary Science Letters*, *doi: 10.1016/j.epsl/2013.05.015*.

Scholl, D. W., and R. von Huene (2007), Crustal recycling at modern subduction zones applied to the past--Issues of growth and preservation of continental basement, mantle geochemistry, and supercontinent reconstruction, in *Geological Society of America, Memoir* edited by J. Robert D. Hatcher, M. P. Carlson, J. H. McBride and J. R. M. Catalán:, pp. 9-32, Geological Society of America, Boulder.

Schwab, M., Ratschbacher, L., Siebel, W., McWilliams, M., Minaev, V., Lutkov, V., et al. (2004), Assembly of the Pamirs: Age and origin of magmatic belts from the southern Tien Shan to the southern Pamirs and their relation to Tibet, *Tectonics, 23*(4).

Simon, L., and C. Lécuyer (2005), Continental recycling: The oxygen isotope point of view, *G-cubed*, *6*, doi:10.1029/2005GC000958.

Sippl, C., B. Schurr, X. Yuan, J. Mechie, F. M. Schneider, M. Gadoev, S. Orunbaev, I. Oimahmadov, C. Haberland, U. Abdybachaev, V. Minaev, S. Negmatullaev, and N. Radjabov (2013), Geometry of the Pamir-Hindu Kush intermediate-depth earthquake zone from local seismic data, *Journal of Geophysical Research, 118*, 1-20.

Stearns, M. A., B. R. Hacker, L. Ratschbacher, J. Lee, J. M. Cottle, and A. Kylander-Clark (2013), Synchronous Oligocene–Miocene metamorphism of the deep Pamir and Himalaya driven by plate-scale dynamics, *Geology*, *41*, 1071-1074.

Stearns, M. A., Hacker, B. R., Ratschbacher, L., Rutte, D., & Kylander-Clark, A. R. C. (2015), Titanite petrochronology of the Pamir gneiss domes: Implications for middle to deep crust exhumation and titanite closure to Pb and Zr diffusion, *Tectonics*, *34*(4), 784-802.

Stern, R. J. (2010), Yin and yang of continental crust creation and destruction by plate tectonic processes, *International Geology Review*, *52*, 1-31.

Stübner, K., L. Ratschbacher, D. Rutte, K. Stanek, V. Minaev, M. Wiesinger, R. Gloaguen, and project TIPAGE members (2013a), The giant Shakhdara migmatitic gneiss dome, Pamir, India–Asia collision zone, 1: Geometry and kinematics, *Tectonics*, *32*, 948-979.

Stübner, K., L. Ratschbacher, C. Weise, J. Chow, J. Hofmann, J. Khan, D. Rutte, B. Sperner, J. Pfänder, B. R. Hacker, I. Dunkl, M. Tichomirowa, M. A. Stearns, and project TIPAGE members (2013b), The giant Shakhdara migmatitic gneiss dome, Pamir, India–Asia collision zone, 2: Timing of dome formation, *Tectonics*, *32*, 1404-1431.

Tamura, Y., O. Ishizuka, K. Aoike, S. Kawate, H. Kawabata, Q. Chang, S. Saito, Y. Tatsumi, M. Arima, M. Takahashi, T. Kanamaru, S. Kodaira, and R. S. Fiske (2010), Missing Oligocene Crust of the Izu-Bonin Arc: Consumed or Rejuvenated During Collision?, *Journal of Petrology*, *51*, 823-846.

Timms, N. E., Kinny, P. D., Reddy, S. M., Evans, K., Clark, C., & Healy, D. (2011), Relationship among titanium, rare earth elements, U–Pb ages and deformation microstructures in zircon: Implications for Ti-in-zircon thermometry, *Chemical Geology*, *280*(1), 33-46.

Taylor, R. J. M., Harley, S. L., Hinton, R. W., Elphick, S., Clark, C., & Kelly, N. M. (2015), Experimental determination of REE partition coefficients between zircon, garnet and melt: a key to understanding high-T crustal processes, *Journal of Metamorphic Geology*, *33*(3), 231-248.

Wang, Y., Foley, S. F., & Prelević, D., (2017), Potassium-rich magmatism from a phlogopite-free source, *Geology*, *45*(5), 467-470.

Wiedenbeck, M. A. P. C., Alle, P., Corfu, F., Griffin, W. L., Meier, M., Oberli, F. V., et al. (1995), Three natural zircon standards for U-Th-Pb, Lu-Hf, trace element and REE analyses, *Geostandards and Geoanalytical Research*, *19*(1), 1-23.

Yin, A., and T. M. Harrison (2000), Geologic evolution of the Himalayan–Tibetan orogen, *Annual Review of Earth and Planetary Sciences*, *28*, 211–280.

Zandt, G., and C. R. Carrigan (1993), Small-scale convective instability and upper mantle viscosity under California, *Science*, *261*, 460-463.

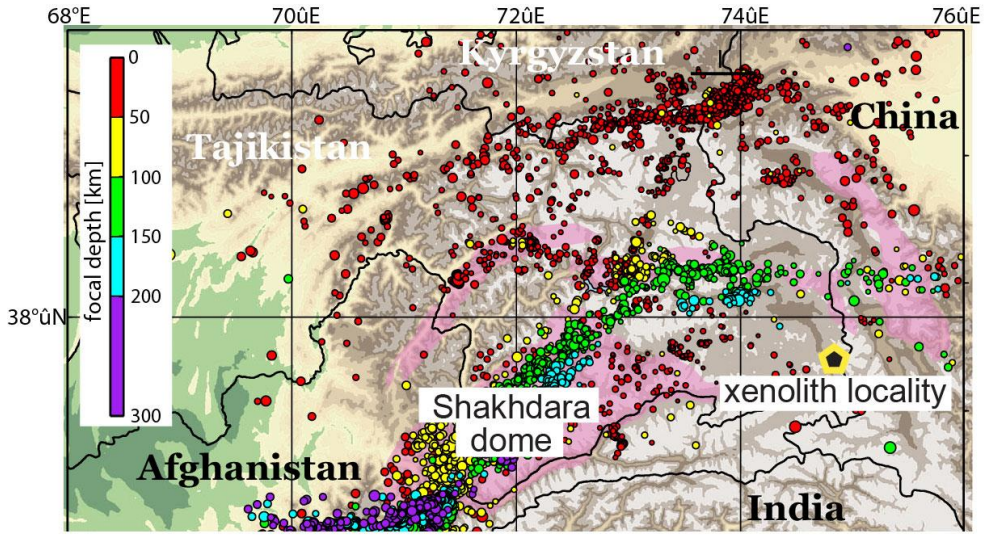

Figure 1. The Pamir are the western extent of the Tibetan Plateau. They are underlain in the North by a S-dipping Asian slab that is seismic (epicenters from *Sippl et al.* [2013] shown by the colored dots), and in the south by a flat-slab segment of the Indian plate. Gneiss domes (pink) expose high-grade Cenozoic rocks throughout much of the Pamir. The xenoliths (star symbol) in the SE Pamir were erupted from mantle depths.

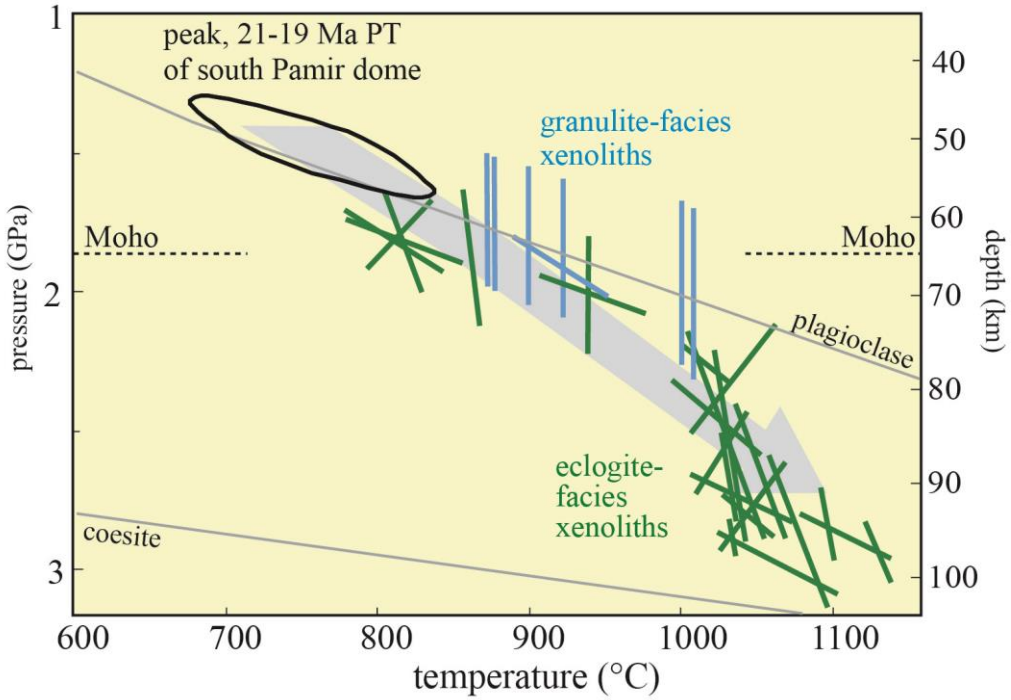

Figure 2. Calculated pressures and temperatures for the eclogite-facies xenoliths (green lines) and high-pressure granulites (blue lines); each line represents the position of a single reaction. Gray arrow: probable PT path. Modified from *Gordon et al.* [2012].

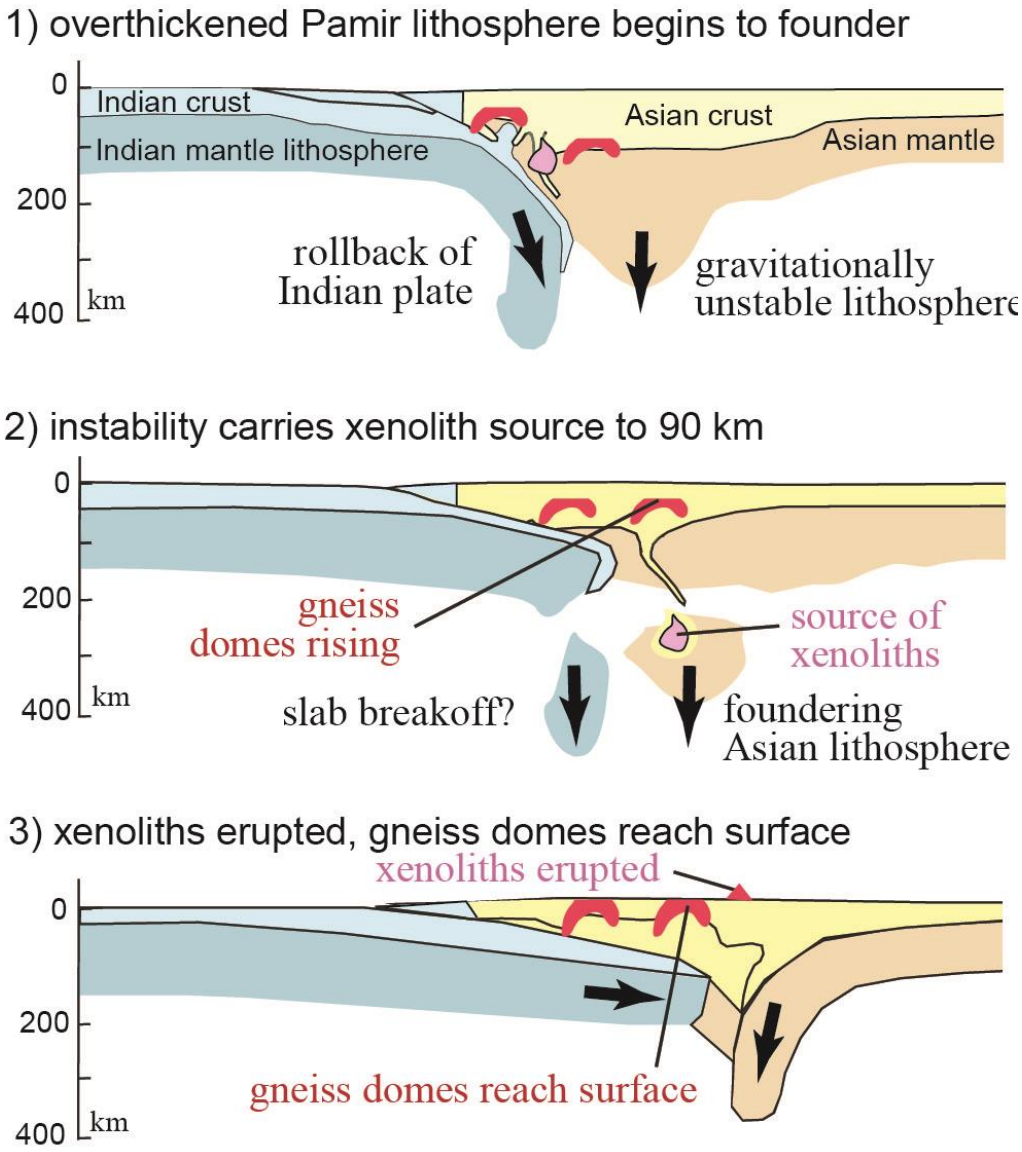

Figure 3. Hypothetical evolution of Pamir orogen.

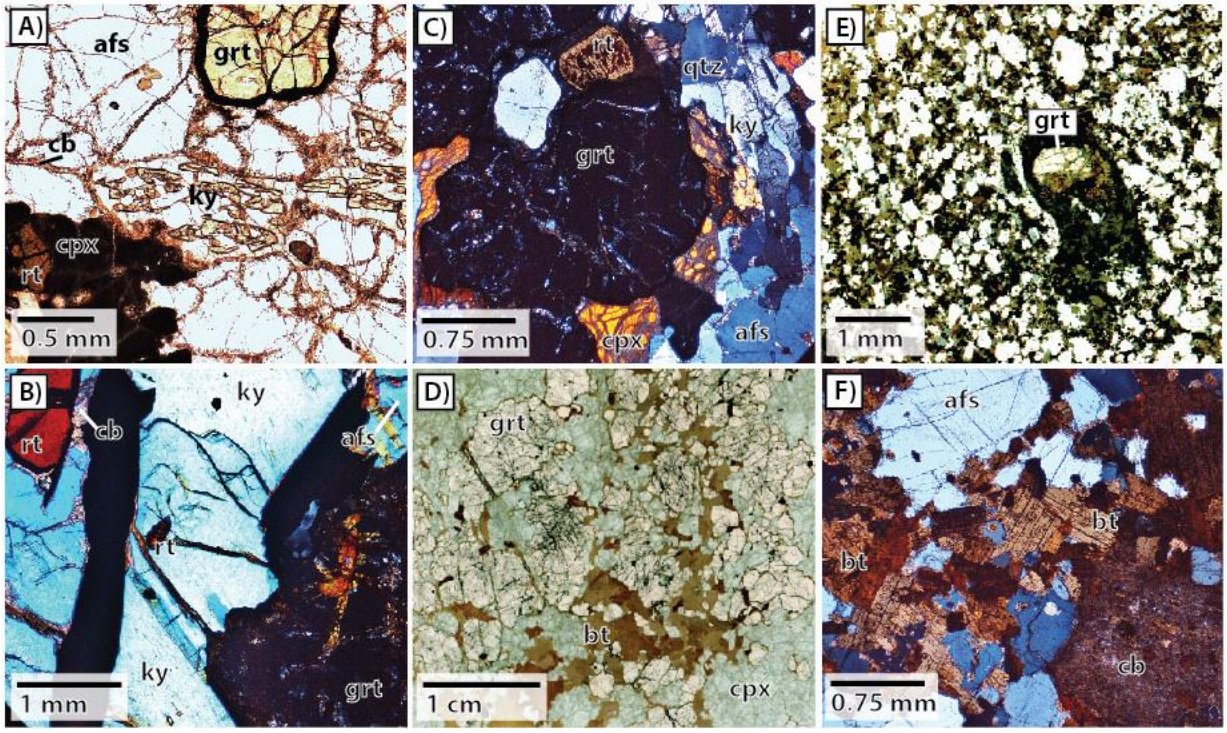

Figure 4. Representative photomicrographs from the Pamir xenoliths. A) K-rich meta-igneous xenolith DK10, with injected carbonate veins among relict kyanite, garnet, alkali feldspar, and clinopyroxene. B) Meta-pelite DK20_2 with very coarse kyanite, garnet, and alkali feldspar, interstitial rutile, and fine-grained carbonate percolating along grain boundaries. C) Meta-igneous xenolith DK3 shows rutile enclosed in garnet, with clinopyroxene and kyanite. D) Mafic xenolith 33* exhibiting crystallization of phlogopite along clinopyroxene and garnet grain boundaries after melt injection. E) DK28 with phenocrystic alkali feldspar and phlogopite, and a garnet xenocryst with a corona of clinopyroxene and "trail of biotite. F) Minette DK36 with globular alkali feldspar, castellated phlogopite, and carbonate groundmass [*Kretz, 1983]*. See also Figure 2 in *Hacker et al.* [2005].

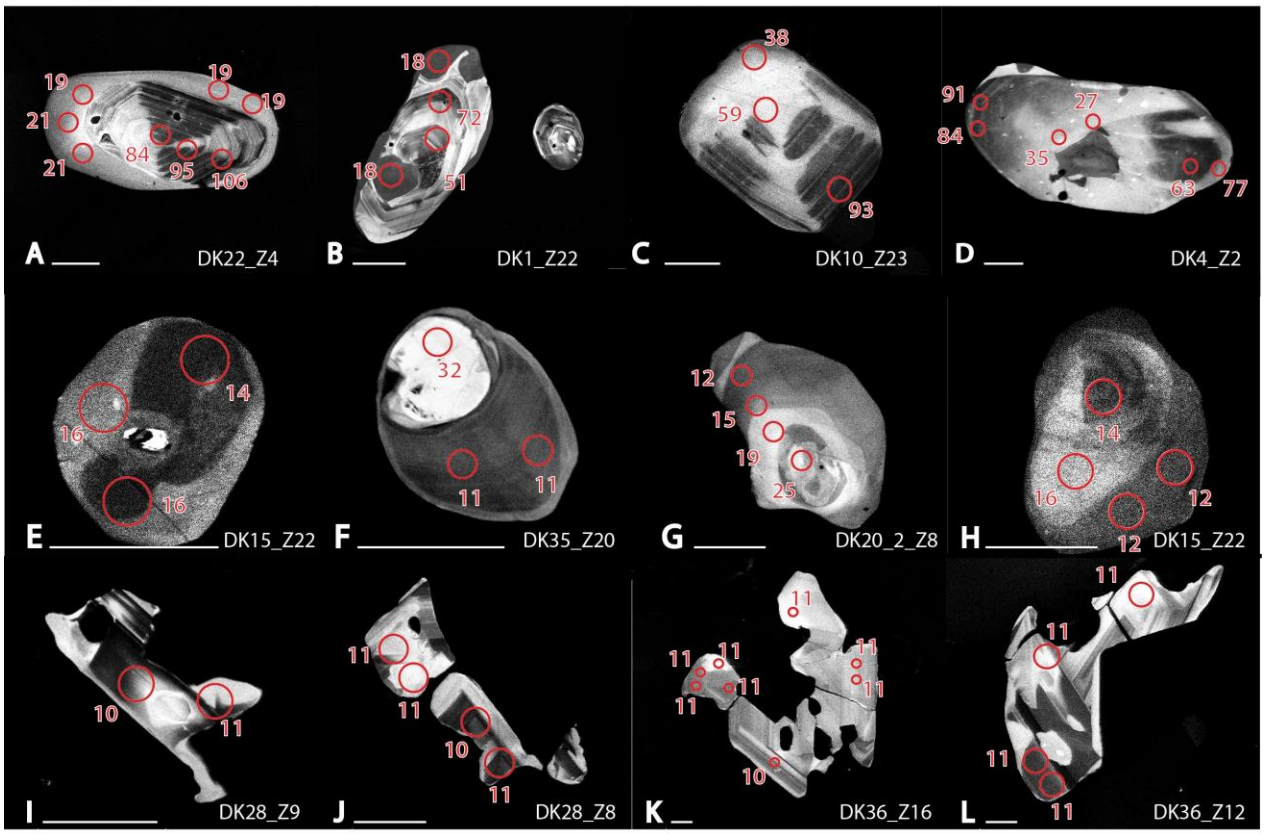

Figure 5. Textures of xenolith zircon. Red circles are 15-um LASS spots and U-Pb dates (Ma). A-D) Igneous protolith xenoliths have subhedral – anhedral grains with oscillatory zoning; metamict domains; recrystallized, complexly shaped domains with CL-flat or ghost zoning; and thin, CL-flat rims. C & D exhibit a transition of magmatic textures to bright CL "ghost-zoning," associated with Paleogene U-Pb dates. E-H) Meta-pelite xenolith zircons are typically anhedral, with poorly preserved to non-existent cores surrounded by wide, CL-flat rims. I-L) Minette zircons are irregular and skeletal, with multiple oscillatorily zoned domains and convoluted recrystallized domains. Scale bars are 50 microns.

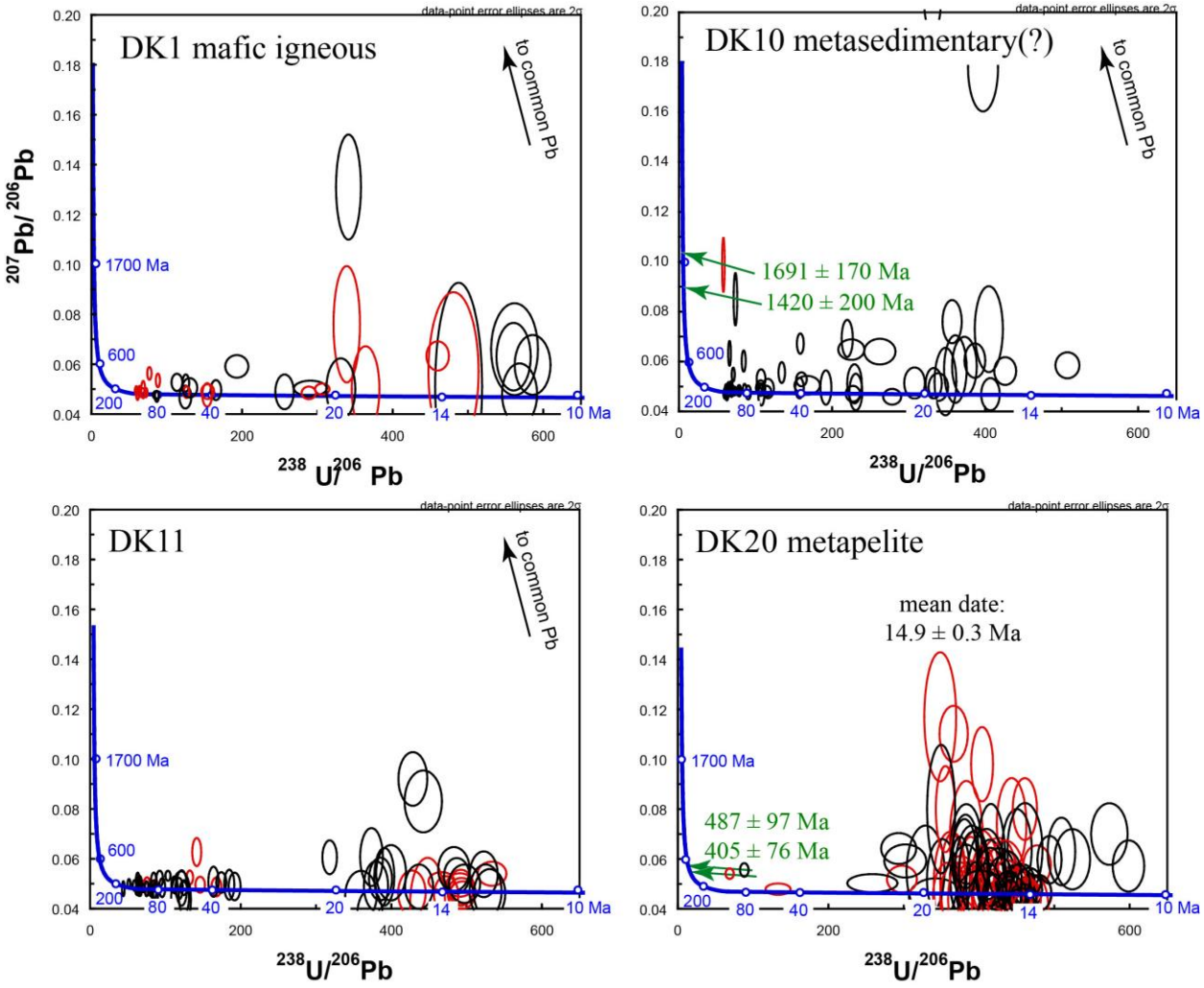

Figure 6. Tera-Wasserburg diagrams for xenolith zircon U-Pb data. Two samples with relatively few data are not included. Zircon that occur as inclusions in other minerals (mostly garnet) are red; matrix grains are black. Zircons that may be inherited are indicated with green text. Ages in Concordia shown in blue.

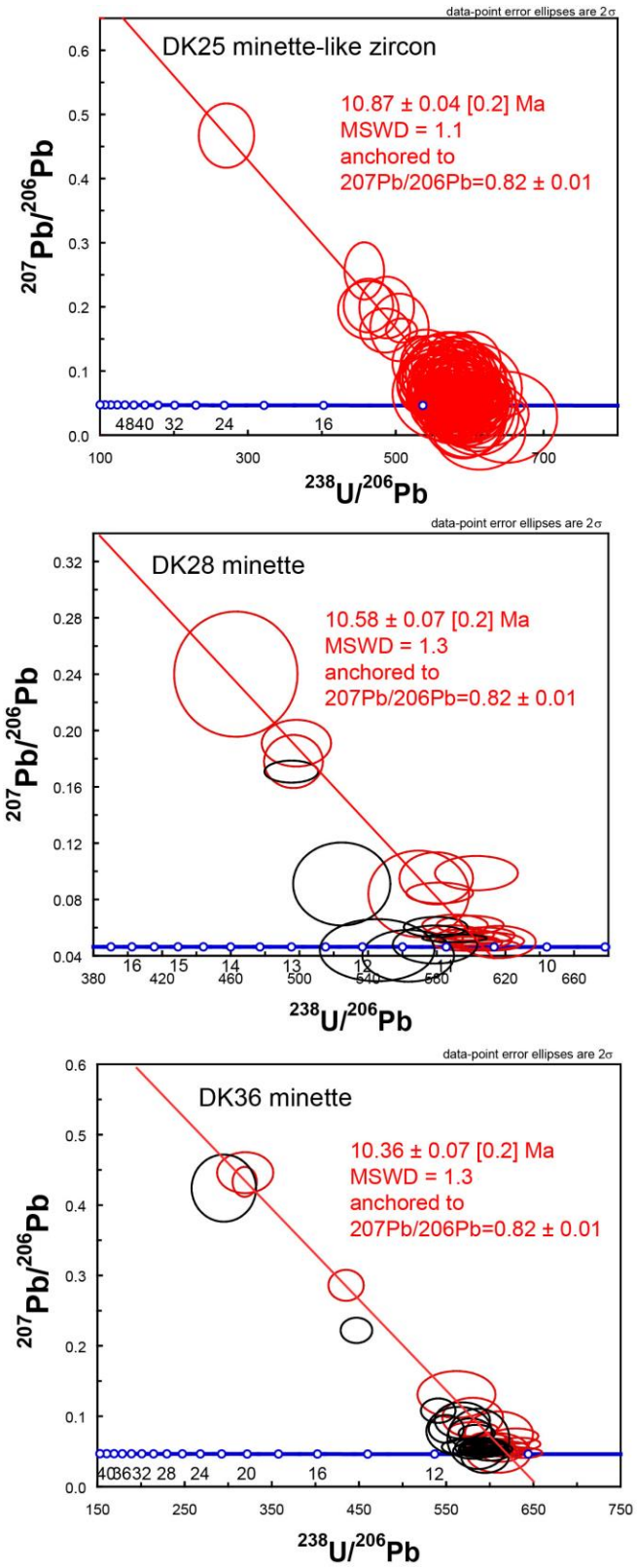

Figure 7. Tera-Wasserburg diagram for minette zircon U-Pb data.

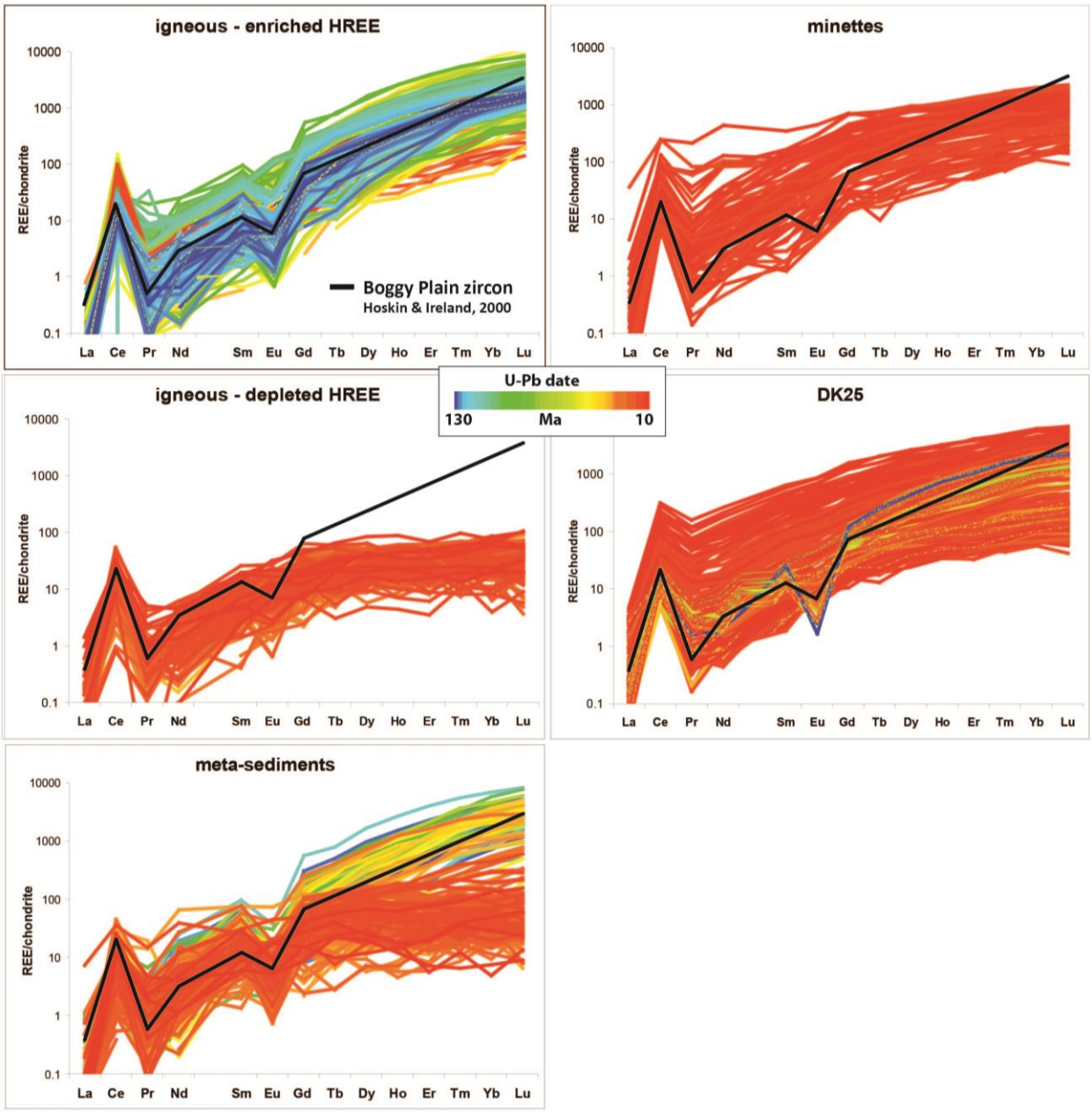

Figure 8. Chondrite-normalized REE for each xenolith type, plus sample DK25. Boggy Plain plutonic zircon average REEs included for reference to typical zircon REE behavior [*Hoskin & Ireland*, 2000]. Cooler colors represent older zircon ages; warmer colors represent younger ages. Crustal xenoliths (left) show depletion in HREEs among the younger zircon zones, as well as changes in Eu/Eu*. Typical Eu/Eu* for older analyses are similar to Boggy Plain zircon. Minette REEs (upper right) show enriched LREEs and less variable REE abundances, and little to no Eu anomaly. DK25 (above) shows older zircon with REEs similar to crustal xenoliths, and younger zircon with REEs similar to minettes.

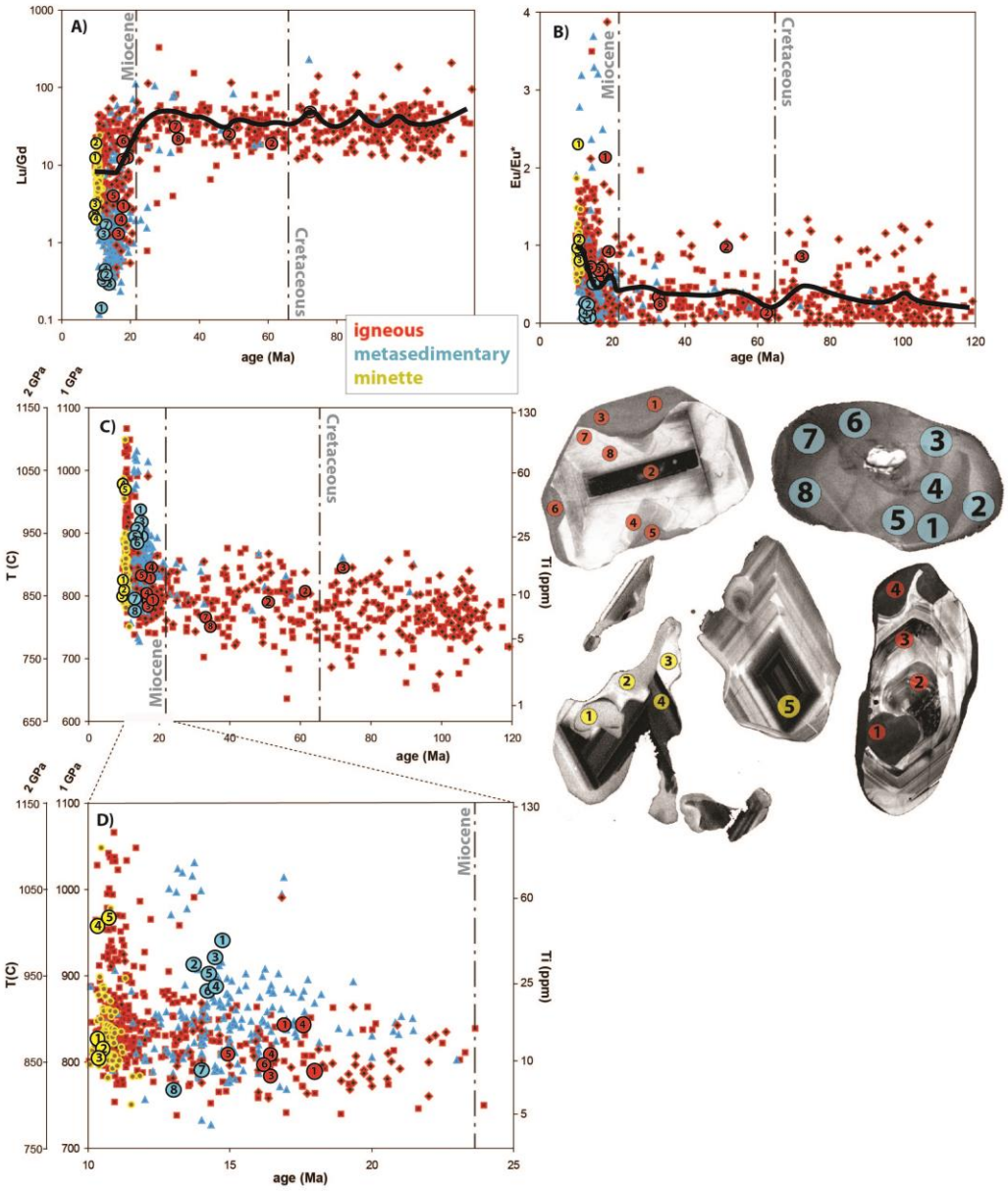

Figure 9. Lu/Gd, Eu/Eu*, Ti concentration, and inferred temperature in zircon. The CL images show locations of 15-um LASS spots, and highlight the differences between zircon core and rim compositions. Numbered spots correspond to those represented on the figures; the four colors represent the four different types of xenolith. A) Lu/Gd ratio; all types of xenolith show significant depletion in HREE at ~20 Ma. B) Eu/Eu* changes from strongly negative Eu anomalies to neutral/positive anomalies near 20 Ma. C&D) Ti-in-zircon temperatures are ~800-850C until ~14 Ma, when they increase to >950-1000C. Heavy black lines in A & B are running averages.

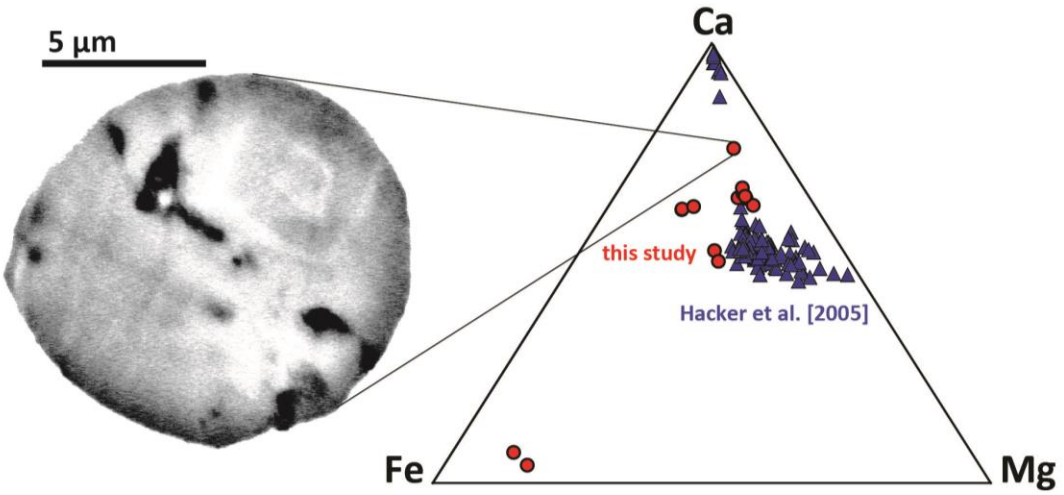

Figure 10. (left) Micron-scale zoning in a ternary carbonate inclusion visible with BSE; energy-dispersive spectrometry showed that the zoning in correlated with changes in Mg/Ca. (right) Ca-Mg-Fe ternary diagram showing compositions of the carbonate inclusions in both this study and *Hacker et al.* [2005].

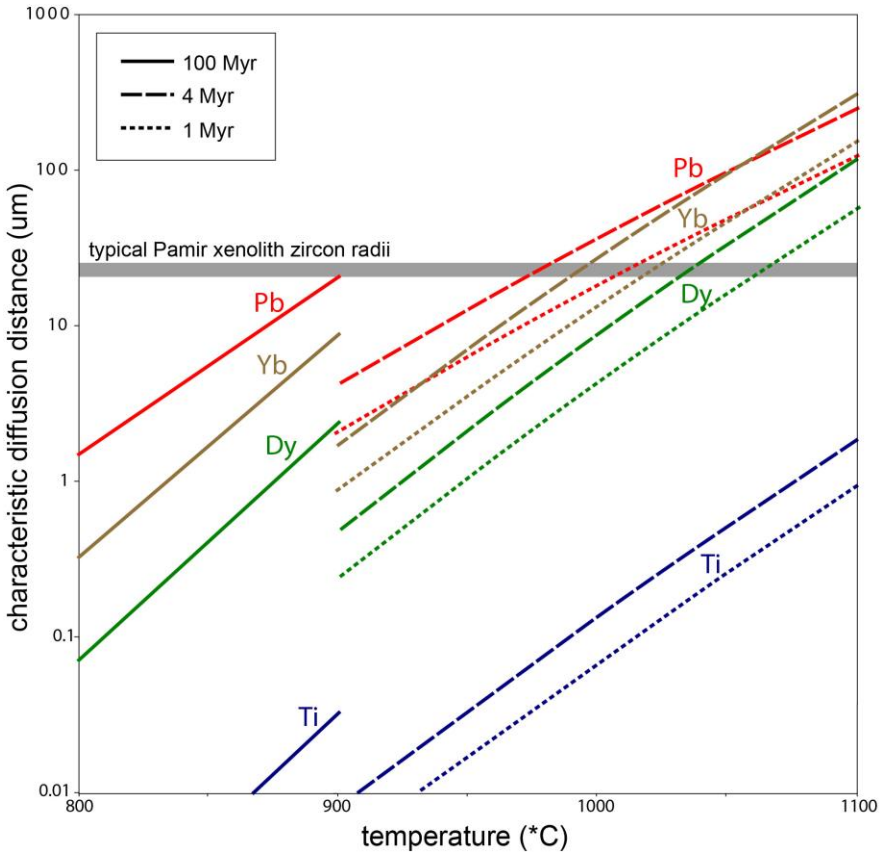

Figure 11. Laboratory diffusion distances of Ti, Dy, Yb, and Pb in zircon over 1-4 Myr [*Cherniak*, 1997; *Cherniak*, 2000].

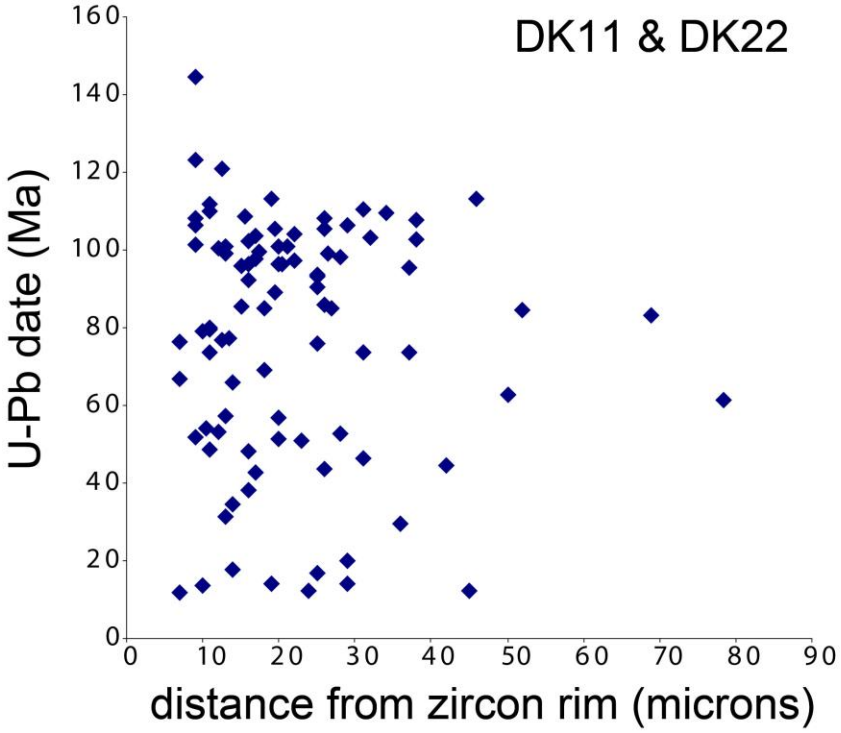

Figure 12. Relationships between zircon age and distance of LASS analysis from zircon rim. No distinct correlation is visible.

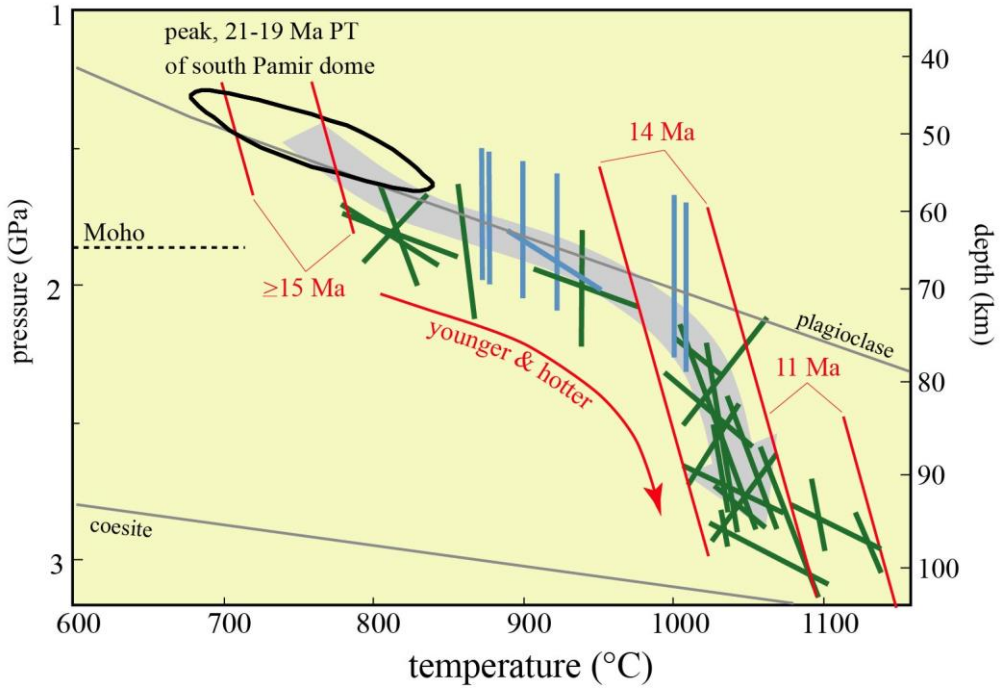

Figure 13. Pressure and temperature evolution of Pamir xenoliths.

Table 1. Summary of U-Pb data.

sample	Protolith	oldest concordant zircon	youngest zircon	summary of dates
DK1	mafic, igneous	107–82 Ma inclusions in garnet	11.8 ± 0.9 Ma	distribution of dates from 107 to 11 Ma
DK2	mafic, igneous	159 ± 6 Ma	14.2 ± 0.5 Ma	bimodal Cretaceous and Miocene
DK3	igneous(?). Minor kyanite	108 ± 2 Ma; n=3	55 ± 2 Ma	entirely Cretaceous
DK4	igneous(?). Minor kyanite	119 ± 4 Ma	27 ± 1 Ma	mostly Cretaceous
DK6	mafic, igneous	128 ± 4 Ma	11.2 ± 0.5 Ma	distribution of dates from 128 to 11 Ma
DK9	igneous(?). Minor kyanite	148 ± 5 Ma	11.1 ± 0.4 Ma	bimodal Cretaceous and Miocene
DK10	metasedimentary(?). Inherited zircons of different age.	107 ± 3 Ma	11.9 ± 0.8 Ma	distribution of dates from 107 to 12 Ma. Two older spots, projected from 10 Ma, have 1691 and 1420 Ma upper intercept dates
DK11	igneous(?). Minor kyanite	145 ± 5 Ma	12.0 ± 0.4 Ma	bimodal Cretaceous and Miocene
DK14	igneous(?). Minor kyanite and inherited zircon.	85 ± 2 Ma	12.1 ± 0.7 Ma	few data. Oldest spot, projected from 10 Ma has 679 Ma upper intercept date
DK15	metapelite	25 ± 3 Ma	11.1 ± 0.4 Ma	almost entirely Miocene. Oldest spot, projected from 10 Ma, has 731 Ma upper intercept date
DK18	igneous. Intermediate composition.	136 ± 7 Ma	15.8 ± 0.7 Ma	bimodal Cretaceous and Miocene
DK19	igneous(?)	58 ± 3 Ma	10.2 ± 0.8 Ma	few data
DK20	metapelite	92 ± 6 Ma	10.6 ± 0.4 Ma	almost entirely Miocene. Oldest spots, projected from 10 Ma, have 487 and 405 Ma upper intercept dates
DK22	igneous(?). Minor kyanite .	121 ± 4 Ma	12.0 ± 0.8 Ma	bimodal Cretaceous and Miocene
DK25	minette-like	70 ± 4 Ma	9.8 ± 0.8 Ma	distribution of dates from 465 to 10 Ma
DK28	Minette	11.8 ± 0.7 Ma	10.0 ± 0.4 Ma	youngest single population: 10.6 ± 0.1 Ma
DK31	mafic, igneous			few data
DK33	metapelite	15 ± 1 Ma	12.3 ± 0.4 Ma	mostly Miocene. Oldest spots, projected from 10 Ma, have 1400 and 1226 Ma upper intercept dates
DK35	metasedimentary(?)	18 ± 1	10.6 ± 0.6 Ma	mostly Miocene. Oldest spot, projected from 10 Ma, has 496 Ma upper intercept date
DK36	minette	11.2 ± 0.4 Ma	9.9 ± 0.4 Ma	youngest single population: 10.4 ± 0.1 Ma
DK60	igneous(?). Minor kyanite	119 ± 4 Ma	13.6 ± 0.6 Ma	mostly Cretaceous

Table 2. DK36 minette bulk-rock composition, compared to Dunkeldik ultrapotassic volcanic rocks [*Malz, 2011*], and minette global average [*Rock, 1991*].

sample	SiO_2	Al_2O_3	TiO_2	FeO*	MnO	MgO	CaO	Na_2O	K_2O	PO_4	CO_2	H_2O	total
DK36	48.2	17.0	1.8	4.6	0.0	4.6	4.3	1.1	11.0	1.4	4.4	1.4	94.1
Dunkeldik volcanics avg.	45.9	11.7	0.98	6.5	0.13	4.3	10.7	0.73	7.7	1.4	--	--	90.0
Minette global avg.	51.5	12.8	1.3	7.3	0.12	7.1	6.7	2.0	5.6	0.95	2.0	2.1	99.4

Supplemental Figure 1. Tera-Wasserberg diagrams for xenolith zircon U-Pb data.

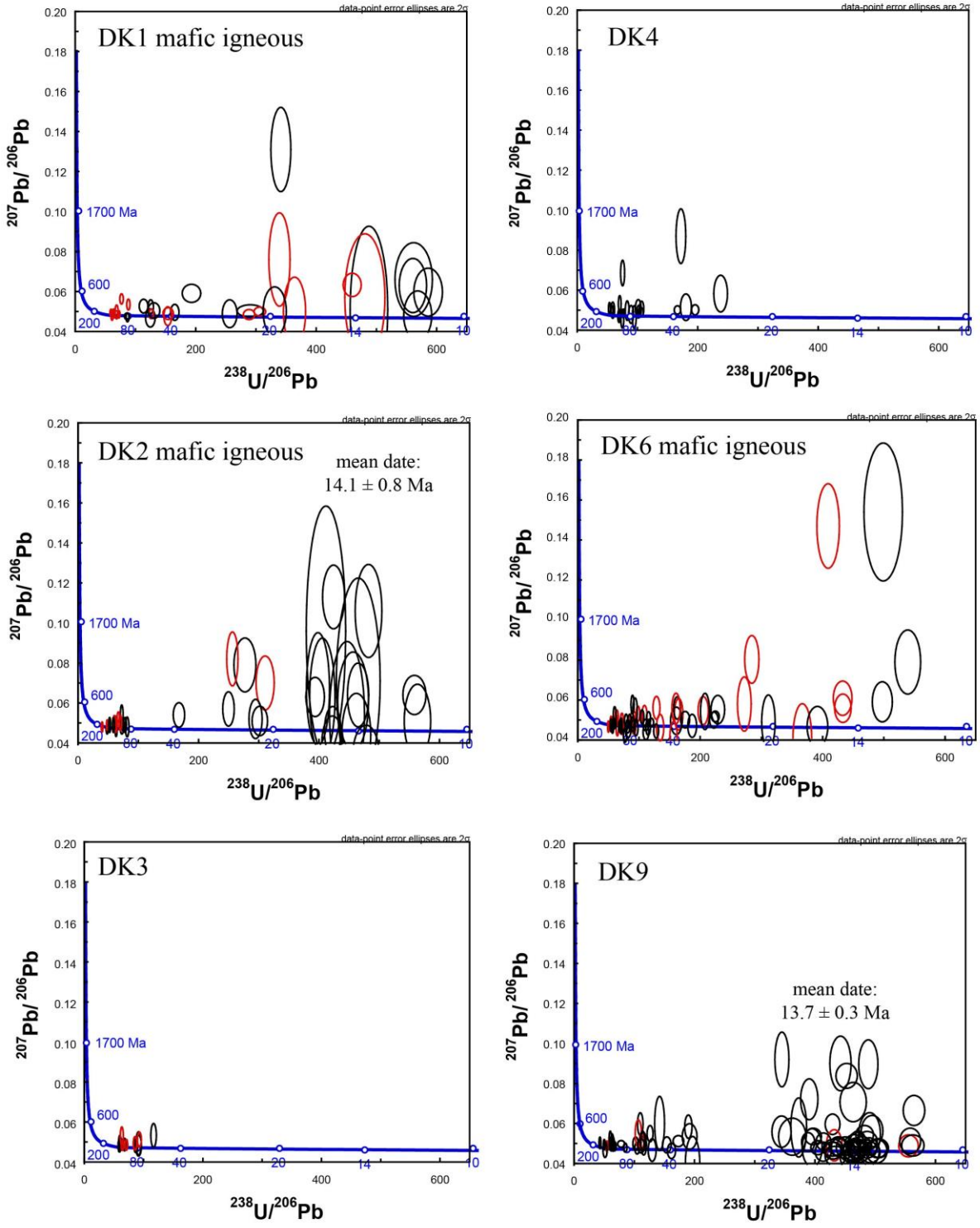

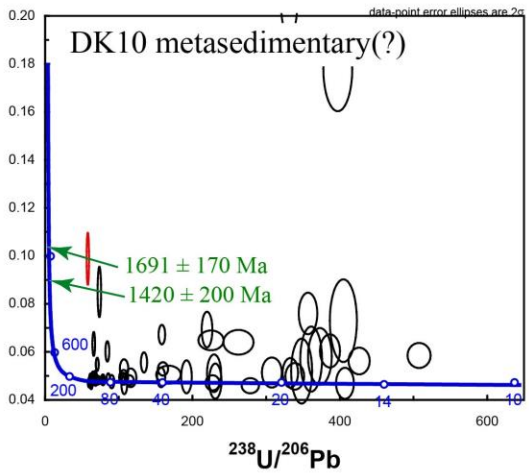
DK10 metasedimentary(?)
data-point error ellipses are 2σ
1691 ± 170 Ma
1420 ± 200 Ma
600
200
80
40
20
14
10
0.20
0.18
0.16
0.14
0.12
0.10
0.08
0.06
0.04
0
200
400
600
238U/206Pb

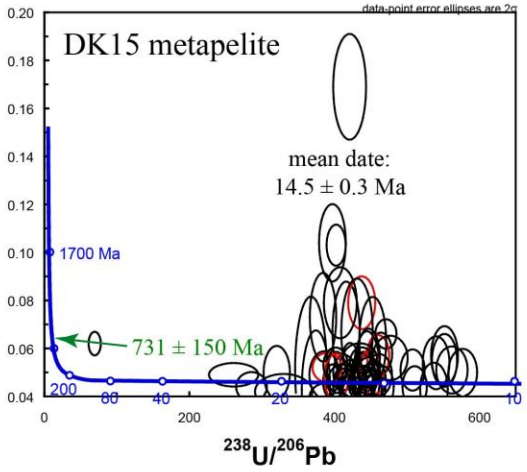
DK15 metapelite
data-point error ellipses are 2σ
mean date:
14.5 ± 0.3 Ma
1700 Ma
731 ± 150 Ma
200
80
40
20
10
0.20
0.18
0.16
0.14
0.12
0.10
0.08
0.06
0.04
0
200
400
600
238U/206Pb

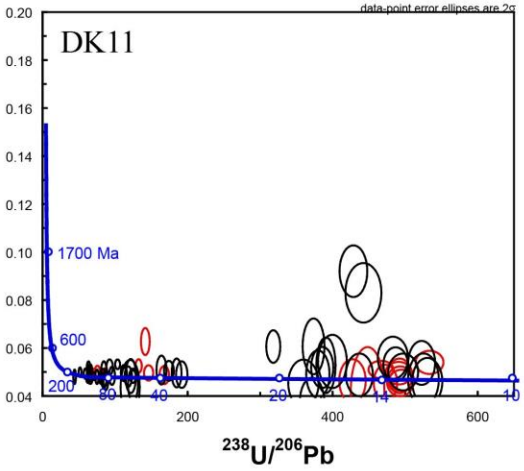
DK11
data-point error ellipses are 2σ
1700 Ma
600
200
80
40
20
14
10
0.20
0.18
0.16
0.14
0.12
0.10
0.08
0.06
0.04
0
200
400
600
238U/206Pb

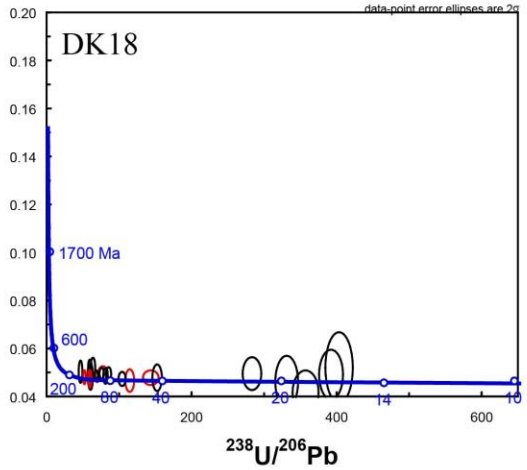
DK18
data-point error ellipses are 2σ
1700 Ma
600
200
80
40
20
14
10
0.20
0.18
0.16
0.14
0.12
0.10
0.08
0.06
0.04
0
200
400
600
238U/206Pb

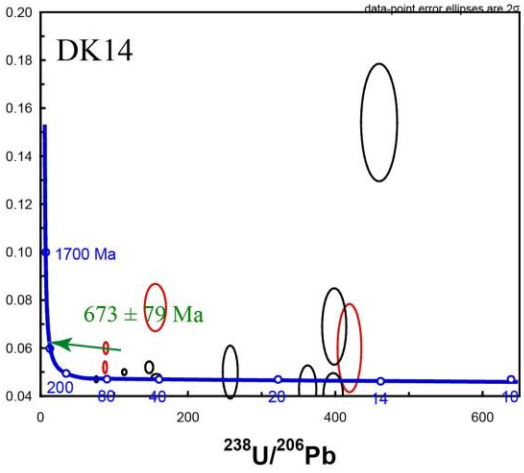
DK14
data-point error ellipses are 2σ
1700 Ma
673 ± 79 Ma
200
80
40
20
14
10
0.20
0.18
0.16
0.14
0.12
0.10
0.08
0.06
0.04
0
200
400
600
238U/206Pb

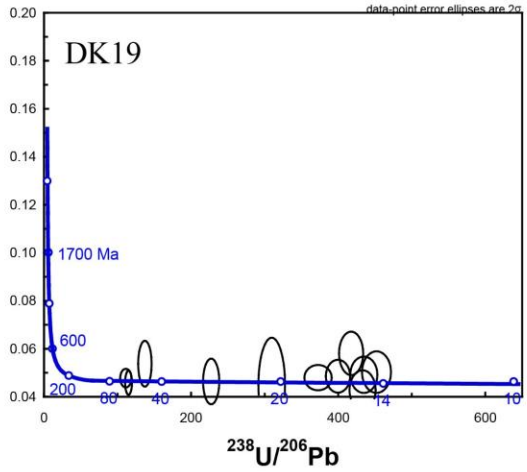
DK19
data-point error ellipses are 2σ
1700 Ma
600
200
80
40
20
14
10
0.20
0.18
0.16
0.14
0.12
0.10
0.08
0.06
0.04
0
200
400
600
238U/206Pb

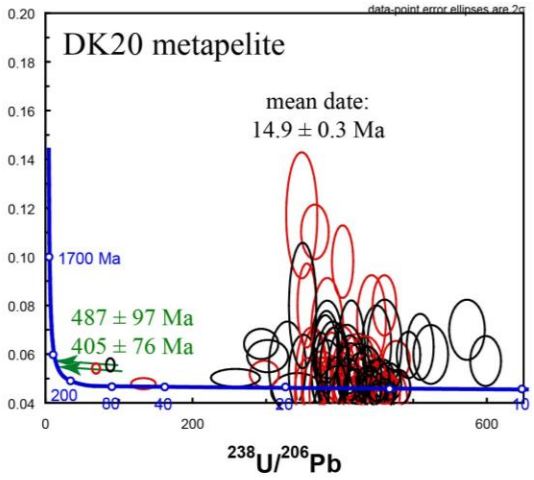
DK20 metapelite
mean date:
14.9 ± 0.3 Ma
1700 Ma
487 ± 97 Ma
405 ± 76 Ma
$^{238}U/^{206}Pb$

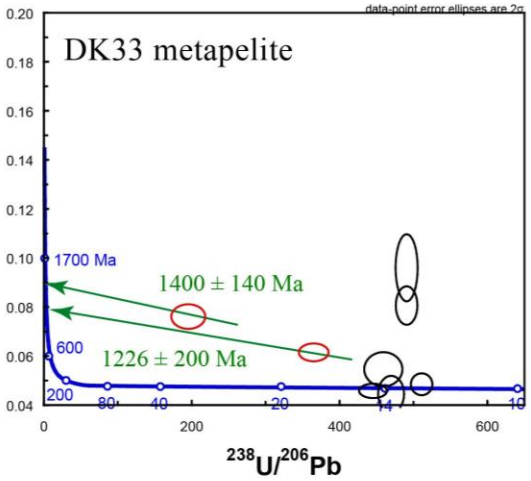
DK33 metapelite
1700 Ma
1400 ± 140 Ma
1226 ± 200 Ma
$^{238}U/^{206}Pb$

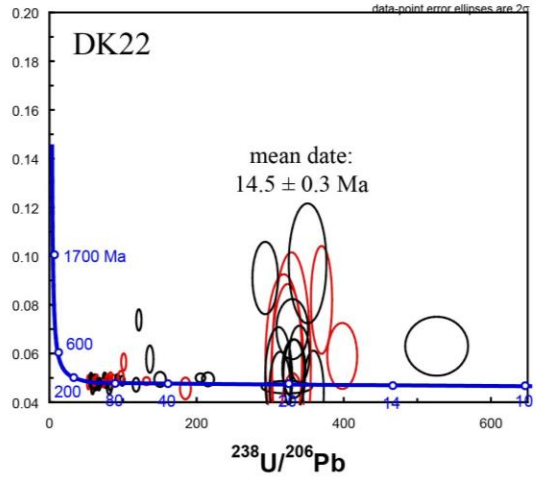
DK22
mean date:
14.5 ± 0.3 Ma
1700 Ma
$^{238}U/^{206}Pb$

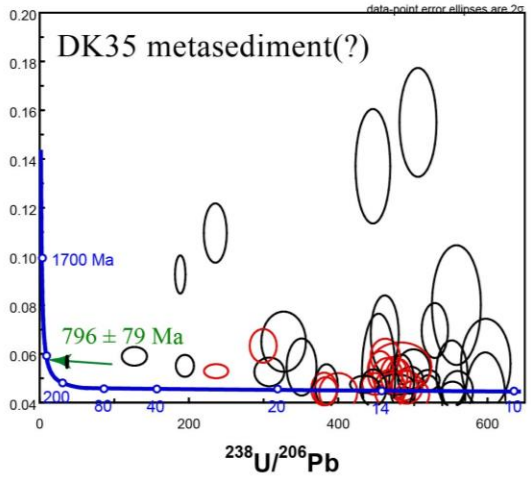
DK35 metasediment(?)
1700 Ma
796 ± 79 Ma
$^{238}U/^{206}Pb$

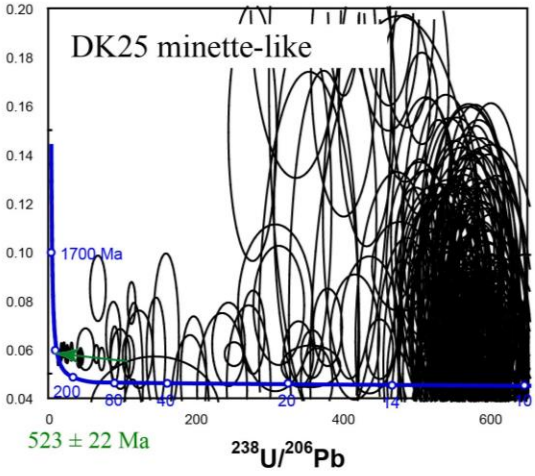
DK25 minette-like
1700 Ma
523 ± 22 Ma
$^{238}U/^{206}Pb$

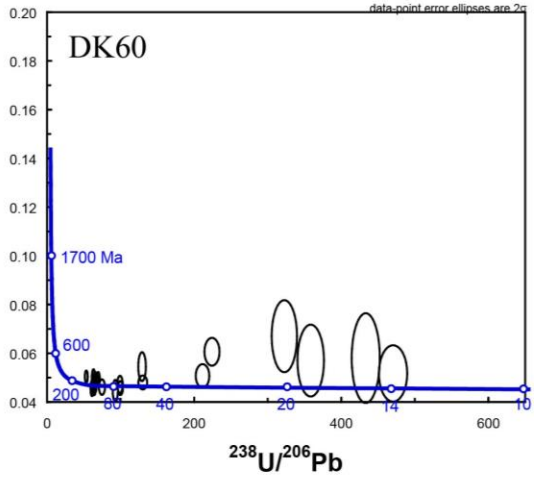
DK60
1700 Ma
$^{238}U/^{206}Pb$

Rock Type	Spot	$^{204}U/^{206}Pb$	2s	$^{207}Pb/^{206}Pb$	2s	Age	±	Ti (ppm)	U.I. date (M	P (GPa)	T	Hofmann	T Ferry &	\Inclusion?	Morphology	Core vs. Rim		La	Ce	Pr	Nd	Sm	Eu	Gd	Tb	Dy	Ho	Er	Tm	Yb	Lu	Eu/Eu*	Lu/Gd
igneous	DK1_Z10_3	585.82	19.38	0.060	0.010	10.8	0.9	29.6		2.5	1110	934	Matric		anhedral, no z rim			0.029536	23.16476	2.478448	0.634573	4.72973	12.43339	44.72362	125.2778	216.6667	379.1209	618.125	971.6599	1366.46	1951.22	0.854876	43.62839
igneous	DK1_Z23_2	661.80	25.35	0.066	0.015	11.2	0.6	19.4		2.5	1057	887	Matric		anhedral, oscil rim			0.067511	8.482871	-0.01918	0.094902	2.5	6.571936	17.35076	20	20.3252	22.89377	19.36032	19.87578	32.11382	1.567061	4.56475	
igneous	DK1_Z10_2	660.54	18.54	0.063	0.011	11.2	0.9	33.7		2.0	1056	924	Matric		anhedral, no z rim	1		0	14.60033	2.165172	2.013129	10.81081	28.41918	33.16583	81.94444	184.9583	336.9963	561.875	866.3969	1124.224	1467.48	1.500849	44.24674
igneous	DK1_Z10_1	568.50	18.97	0.048	0.010	11.3	0.7	31.5		2.0	1047	916	Matric		anhedral, no z rim	2.302586		0	17.94454	1.584052	0.612591	8.648649	22.73536	49.24623	113.3333	233.7398	417.5824	630	951.417	1198.758	1574.797	1.101643	34.00863
igneous	DK1_Z11_2	467.57	25.47	0.051	0.024	13.1	0.9	9.1		2.0	906	787	Matric		anhedral, sligh rim			0.088908	9.352365	0.982089	0.2407	2.557568	6.748556	12.0603	14.44444	19.9187	15.56777	19.125	14.97976	20.49899	30.89431	1.212928	2.581653
igneous	DK1_Z8_1	480.77	27.18	0.057	0.026	13.2	0.9	12.8		2.0	942	820	Garnet		anhedral, no o rim			0.063291	7.814029	0.004483	0.909628	2.5	6.571936	11.55779	26.66667	28.86179	29.30403	43.125	29.55486	40.37267	47.56098	1.222604	4.115058
igneous	DK1_Z25_2	459.77	12.21	0.063	0.005	13.7	1.0	14.2		2.0	953	830	Garnet		anhedral, osc rim?			0.025316	13.05057	0.172414	0.4814	5.202703	13.67673	40.20101	105	219.1057	404.7619	661.875	1080.972	1571.429	2138.211	0.945691	53.18801
igneous	DK1_Z11_1	341.30	13.50	0.131	0.017	16.9	1.0	59		2.0	1132	995	Matric		anhedral, sligh core			0.843882	15.00816	2.801724	1.291028	3.513514	9.236234	36.1809	101.9444	181.3008	329.6703	581.25	914.9798	1173.913	1711.382	0.81919	47.3007
igneous	DK1_Z21_4	364.03	15.00	0.050	0.014	17.6	0.8	15.6		2.0	964	839	Garnet		anhedral, oscil rim			0.025316	6.867863	1.185345	0.857155	2.22973	5.861466	19.09548	27.22222	63.82114	98.9011	158.125	222.6721	335.4037	357.7236	0.898285	18.73342
igneous	DK1_Z21_5	338.98	14.34	0.076	0.019	18.3	0.9	9.3		2.0	999	799	Garnet		anhedral, oscil rim			0.088608	1.712897	0.301724	0.2407	1.756757	4.618117	2.663317	6.388889	13.41463	17.76557	24.375	27.12551	41.81481	31.30081	2.134999	11.75257
igneous	DK1_Z32_2	331.13	15.72	0.050	0.010	19.4	1.0	18.9		2.0	985	850	Matric		anhedral, grun rim			0	7.830343	0.614224	0.392873	4.054054	10.85719	9.949246	16.66667	34.14634	53.47985	84.375	131.9838	200.6211	292.6829	1.166554	29.71528
igneous	DK1_Z26_2	308.47	7.78	0.050	0.002	20.9	0.5	15.2		2.0	961	837	Garnet		anhedral, metz core			0.084388	3.409462	0.540569	3.282276	28.37838	74.60036	156.2965	361.1111	646.3415	1078.755	1518.75	2380.567	2937.888	3869.919	1.109543	24.29381
igneous	DK1_Z23_1	290.70	17.87	0.050	0.003	22.0	1.4	12.8		2.0	942	820	Matric		anhedral, osci core			0.029536	23.16476	2.165172	1.969365	20.27027	53.28597	144.2211	291.6667	585.3659	961.5385	1493.75	2275.304	3080.745	3662.602	0.985527	25.39574
igneous	DK1_Z25_1	288.60	7.69	0.049	0.002	22.2	0.6	13.5		2.0	948	825	Garnet		subhedral, osc core			0.025316	24.63295	1.163793	1.159737	10.33784	27.17584	90.46226	181.3889	362.1138	639.1941	1112.5	1829.96	2466.839	2926.829	0.888707	32.35772
igneous	DK1_Z32_1	256.41	9.97	0.049	0.006	25.0	2.4	14.5		2.0	956	832	Matric		anhedral, grun core			0	4.632963	0.646552	0	1.418919	3.730018	7.98995	23.88889	60.1626	136.2637	248.75	421.0526	695.6522	998.374	1.107797	112.488
igneous	DK1_Z16_1	193.05	12.54	0.059	0.004	32.8	2.1	17.3		2.0	975	850	Matric		anhedral, very core			0.227848	11.30696	0.646552	0.875274	4.932432	12.96626	44.72362	113.0556	245.935	419.4139	600	1113.36	1459.627	1882.114	0.973002	42.08322
igneous	DK1_Z32_3	166.29	5.70	0.050	0.003	38.7	1.3	15.5		2.0	963	839	Matric		anhedral, grun core			0.130802	7.177814	0.3125	1.028446	8.445946	22.20249	43.71859	100	200	362.6374	643.75	1048.583	1469.627	1906.504	1.155432	43.60954
igneous	DK1_Z8_3	154.32	6.92	0.049	0.002	41.5	1.9	3.7		2.0	822	710	Garnet		anhedral, no o core			0	6.574225	0.323276	0.371991	2.702703	7.104796	25.62614	77.5	128.8618	263.7363	461.25	716.5992	1024.845	1398.374	0.853678	54.564
igneous	DK1_Z8_2	153.81	5.24	0.048	0.004	41.8	1.5	3.9		2.0	827	715	Garnet		anhedral, no o core			0	7.030995	0.484914	1.115974	3.513514	9.236234	24.62312	59.72222	141.0569	252.7473	425	659.919	925.6638	1266.098	0.993009	51.01294
igneous	DK1_Z30_2	130.55	8.10	0.051	0.003	49.0	3.1	15.7		2.0	964	840	Matric		anhedral, grun rim			0	13.05057	1.400862	1.159737	9.054054	23.80107	38.69347	80.55556	142.2764	232.6007	312.5	483.1984	577.6398	772.3577	1.271616	19.98093
igneous	DK1_Z21_1	126.10	3.16	0.049	0.002	50.8	1.4	8.3		2.0	904	785	Garnet		anhedral, osci core			0.042194	19.41272	1.077598	2.100656	17.22973	45.29307	119.0955	258.3333	532.5203	919.4139	1325	2222.672	2937.888	3642.276	0.999673	30.58283
igneous	DK1_Z31_1	125.31	3.66	0.052	0.003	50.9	1.6	10.7		2.0	923	802	Matric		anhedral, osci core			0.07173	8.640007	2.583995	0.949019	9.391892	24.68917	66.33166	141.9667	273.5772	454.2125	743.75	1275.304	1746.342	2247.967	0.989167	33.89981
igneous	DK1_Z16_3	124.69	6.41	0.047	0.004	51.5	2.7	14.4		2.0	955	831	Matric		anhedral, very rim (slight overlap?)			0.050633	10.27732	0.431034	0.131291	3.986486	10.47957	25.62614	46.38889	117.4797	148.3516	269.375	459.6356	527.9503	784.5528	1.036788	30.61294
igneous	DK1_Z7_1	113.51	5.87	0.053	0.003	56.1	3.0	10		2.0	916	795	Matric		sub- anhedral, core			0.092827	10.44046	3.017241	3.413567	21.89189	57.54885	122.1106	255.8333	500	851.6484	1375	1935.223	2770.186	3268.293	1.113059	26.76503
igneous	DK1_Z21_2	88.26	2.21	0.054	0.002	72.1	1.9	16		2.0	966	842	Garnet		anhedral, oscil core			0.278481	16.47635	0.1831 9	0.984683	5.743243	15.09769	53.76884	157.5	310.9756	600.7326	912.5	1522.267	1900.621	2556.911	0.859145	47.55376
igneous	DK1_Z5_1	86.81	2.03	0.047	0.002	73.9	1.8	2.8		2.0	798	689	Matric		anhedral, no o core			0.021097	5.236642	0.387931	0.175055	4.256757	11.19005	16.58291	45.83333	89.8374	163.1502	348.125	668.0162	1043.478	1430.894	1.331971	86.28726
igneous	DK1_Z8_1	85.91	3.42	0.048	0.001	74.6	3.3	12.5		2.0	939	817	Matric		anhedral, grun core			0.075949	11.23874	0.150862	0.042042	4.324324	11.38767	21.10553	54.44444	84.55528	403.4029	800	1429.15	2161.491	2943.089	1.189911	139.4464
igneous	DK1_Z17_1	78.92	2.35	0.056	0.002	82.4	2.9	14.2		2.0	953	830	Garnet		anhedral, sub-anhedral, core			0.248945	20.71778	2.801724	4.091904	36.48649	95.91474	217.0954	455.5556	873.9837	1523.81	2281.25	3352.227	4236.025	5406.504	1.077715	24.90496
igneous	DK1_Z17_2	72.20	1.75	0.049	0.001	88.6	2.4	7.6		2.0	889	771	Garnet		sub-anhedral, core			0.046414	20.06525	1.831897	0.4814	8.243243	21.66963	66.33166	183.3333	330.4878	611.7216	1006.25	1587.045	2086.957	2833.333	0.926706	42.71455
igneous	DK1_Z27_2	68.73	2.11	0.050	0.003	92.9	3.2	9.7		2.0	913	793	Garnet		subhedral, osc core			0.253165	9.499184	0.678879	0.393873	6.013514	15.80817	59.29146	122.2222	232.9268	430.4029	739.375	1133.603	1565.217	2040.65	0.844335	35.00771
igneous	DK1_Z27_1	67.16	3.77	0.049	0.001	95.2	5.5	5.9		2.0	864	749	Garnet		subhedral, osc core			0.080169	14.35563	-0.0361	0.962801	11.48649	30.19538	59.79899	176.3889	375.2033	633.6996	1056.25	1708.502	2211.18	2882.114	1.152126	48.19669
igneous	DK1_Z9_1	63.94	1.50	0.049	0.001	99.9	2.9	9.5		2.0	911	791	Garnet		anhedral, osci core			0.050633	17.46514	1.293103	0.787746	9.864865	25.9325	74.37186	170	320.3252	564.1026	937.5	1461.538	2049.478	2479.675	0.957403	33.34157
igneous	DK1_Z16_4	61.24	1.48	0.048	0.002	104.4	3.1	6.4		2.0	872	756	Garnet		anhedral, osci core			0.021097	12.0778	33.405 17	1.181619	7.905405	19.45238	81.40704	152.5	321.1382	525.641	875	1404.858	2066.323	2626.016	1.071042	32.25785
igneous	DK1_Z15_2	59.52	1.37	0.049	0.001	107.2	3.1	9.1		2.0	906	787	Garnet		anhedral, osci core			0.172996	15.66069	3.232759	4.223195	40.54054	106.5719	172.8643	463.8889	878.0488	1430.044	2167.5	3060.729	3857.143	5000	1.27305	28.92442
										2.0																						
igneous	DK18_Z7_4	403.39	15.45	0.052	0.012	15.8	0.7	10.4		2.0	920	800	Matric		anhedral, no o rim			0.046414	4.97553	0.44181	0.568928	5.202703	6.927176	6.532663	13.61111	22.76423	28.57143	27.5	21.05263	34.78261	41.05691	1.188219	6.284866
igneous	DK18_Z7_3	392.31	13.45	0.049	0.008	16.4	0.7	5.9		2.0	864	749	Matric		anhedral, no o rim			0.030802	5.858444	0.786638	0.2407	2.027027	7.815275	17.58794	34.44444	24.79675	36.99634	35.625	31.17409	40.99379	57.31707	1.306902	3.256885
igneous	DK18_Z9_1	367.14	14.82	0.042	0.008	18.1	0.8	11.3		2.0	929	808	Matric		anhedral, no o rim			0.029536	12.73431	1.185345	0.964963	10.94595	11.36767	50.45226	200	333.7398	613.8531	825	1336.032	1552.795	1866.179	0.961273	20.85776
igneous	DK18_Z9_3	331.13	12.81	0.046	0.009	19.4	0.8	10.4		2.0	920	800	Matric		anhedral, no o rim			0.013924	6.101142	0	0.437637	4.72973	0.657194	13.56784	16.66667	37.80488	50.3663	46.875	47.36842	69.56522	89.43089	0.982039	6.591388
igneous	DK18_Z8_2	283.29	10.49	0.050	0.005	22.6	0.9	14.1		2.0	953	829	Matric		anhedral, no o rim (possible overlap)			0.010549	26.00326	0.3125	1.247265	7.635135	9.236234	27.63819	63.33333	65.85366	97.0696	127.5	174.4939	234.7826	317.0732	0.635616	11.47228
igneous	DK18_Z5_1	152.44	5.37	0.048	0.005	42.1	1.5	9.5		2.0	911	791	Matric		anhedral, extre core			0.012658	17.29201	0	3.063457	9.459459	2.131439	53.26633	136.1111	273.9837	452.381	756.25	1149.798	1608.696	1788.618	0.094954	33.57877
igneous	DK18_Z3_5	143.68	8.74	0.048	0.002	44.7	2.8	10.9		2.0	925	804	Garnet?		anhedral, no o core			0.033755	25.61175	0.969828	12.25383	15.81081	9.591474	104.5226	206.6667	360.5691	597.0696	900	1384.615	1782.609	1939.024	0.236941	18.55124
igneous	DK18_Z3_3	114.88	5.03	0.047	0.004	56.0	2.5	10.3		2.0	919	799	Garnet?		anhedral, no o core			0.013924	15.82382	1.400862	0.415755	7.635135	3.730018	27.13568	86.11111	196.748	316.6813	525	850.2024	1140.068	1471.545	0.259139	54.22915
igneous	DK18_Z5_2	104.17	4.05	0.047	0.004	61.6	2.6	14.5		2.0	956	832	Matric		anhedral, no o core			0.011392	27.23227	5.387931	3.928932	29.72973	13.55784	355.5556	621.1111	1097.561	1497.5	2263.16	2545.894	3063.496	3155.538	0.228002	8.861521
igneous	DK18_Z5_6	85.54	2.90	0.049	0.002	74.8	2.9	15.6		2.0	964	839	Matric		anhedral, extre core			0.042194	20.39152	1.831897	4.704595	40.54054	9.058615	147.2362	300	504.065	869.9634	1406.25	2004.049	2472.05	2918.699	0.117249	19.82325
igneous	DK18_Z4_2	81.30	2.51	0.049	0.003	78.7	2.8	12.7		2.0	941	819	Matric		anhedral, no o core			0.011814	15.66069	0	0.59081	16.89189	13.14387	90.45226	155.5556	255.4472	500	818.75	1089.069	1484.472	1825.203	0.336259	20.17964
igneous	DK18_Z3_6	77.70	5.30	0.050	0.002	82.2	5.7	11.9		2.0	934	812	Garnet?		anhedral, no o core			0	14.66558	1.724138	0.897155	2.432432	4.065258	32.1608	62.77778	134.9593	228.9377	407.5	599.1903	881.9876	1117.886	0.461887	34.75927
igneous	DK18_Z5_5	75.99	2.53	0.050	0.002	84.1	3.3	10.5		2.0	921	800	Matric		anhedral, extre core			0.054852	29.69005	4.525862	6.345733	40.54054	15.98579	201.005	400	695.122	1126.374	1650	2457.49	3006.211	3361.789	0.177087	16.7249
igneous	DK18_Z3_4	69.78	2.20	0.049	0.001	91.7	3.4	19		2.0	966	842	Garnet?		anhedral, no o core			0.037975	15.66069	2.262931	6.129914	32.77027	13.1008	241.4866	413.8889	1375	2157.652	2503.106	2902.439	0.130795	21.98142
igneous	DK18_Z5_3	68.45	2.00	0.049	0.001	93.4	2.7	6.2		2.0	869	752	Matric		anhedral, extre core?			0	19.08646	1.616379	-0.00365	9.851351	1.598579	30.65327	78.33333	195.5285	388.2784	687.5	1161.948	1819.876	2357.724	0.097048	76.9159
igneous	DK18_Z8_4	63.90	2.58	0.052	0.003	99.6	4.5	13.8		2.0	950	827	Matric		anhedral, no o core			0.067511	10.08157	0.646552	1.991247	12.97297	7.282416	61.30653	137.5	278.8618	421.2454	601.25	902.834	1211.18	1402.439	0.258227	22.87585
igneous	DK18_Z4_5	61.09	1.84	0.050	0.003	104.4	3.7	10.8		2.0	924	803	Matric		anhedral, no o core			0.022363	18.59706	2.155172	3.282276	10.81081	1.953819	64.32161	166.6667	328.8618	479.8535	806.25	1218.623	1466.839	1727.642	0.074093	26.85944
igneous	DK18_Z7_1	60.63	2.51	0.047	0.003	105.8	4.8	12.9		2.0	943	820	Matric		anhedral, no o core			0.029536	13.33768	1.724138	1.838074	22.97297	12.96626	66.33166	169.4444	304.878	501.8315	706.25	1113.36	1453.416	1825.203	0.332159	27.51632
igneous	DK18_Z4_1	59.70	1.89	0.052	0.003	106.5	4.0	11.6		2.0	932	810	Matric		anhedral, no o core			0	11.41925	0.377155	2.472646	8.216216	3.019538	64.32161	99.16667	203.252	390.1099	695	959.5142	1254.658	1609.756	0.151006	25.02668
igneous	DK18_Z3_1	59.81	1.51	0.047	0.003	107.0	3.5	4.1		2.0	831	719	Garnet		anhedral, no o core			0	15.66069	1.077598	1.197516	9.324324	5.927176	52.31156	140.7222	308.9024	487.1795	758.75	1161.948	1509.317	1925.829	0.287384	30.92265
igneous	DK18_Z9_4	59.49	1.62	0.048	0.002	107.4	3.7	6.6		2.0	875	758	Garnet		anhedral, no o core			0	16.47635	2.047414	9.190372	53.37838	20.42629	202.0101	366.6667	686.9919	1025.641	1406.25	1987.854	2534.161	2849.593	0.196707	14.1062
igneous	DK18_Z7_2	59.24	2.15	0.049	0.004	107.8	4.4	14.8		2.0	958	834	Matric		anhedral, no o core			0.011814	10.75672	0.75431	0.743982	4.054054	2.664298	45.72864	96.11111	233.7398	373.6264	581.875	862.3482	1130.435	1516.26	0.196679	33.15778
igneous	DK18_Z9_2	52.16	1.41	0.048	0.002	122.5	4.3	7		2.0	881	763	Garnet		anhedral, no o core			0.07173	11.68026	0.355603	1.563611	12.16216	7.815275	51.5075	159.1667	259.7561	441.3919	696.25	1263.158	1466.839	1609.756	0.222428	15.85849
igneous	DK18_Z8_5	46.82	2.10	0.050	0.004	136.0	6.6	13.7		2.0	949	826	Matric		anhedral, no o core			0.050633	11.41925	1.196346	2.035011	5.27027	5.150977	32.1608	109.7222	193.9024	293.0403	512.5	769.2308	987.5776	1252.033	0.396849	38.93039
										2.0																						
igneous	DK2_Z8_4	558.35	15.61	0.064	0.008	11.3	0.6	15		2.0	959	835	Matric		anhedral, hom rim			0.097046	35.23654	1.303879	0.875274	10.27027	18.29495	23.61809	66.11111	102.439	203.2967	362.5	514.17	801.2422	900.813	1.174669	33.90876
igneous	DK2_Z8_1	563.38	17.94	0.051	0.015	11.4	0.5	11.6		2.0	932	810	Matric		anhedral, hom rim			0.080169	27.56933	0.49569	0.437637	4.527027	9.236234	52.76382	97.22222	207.7236	318.6813	525	688.2591	1018.634	1223.577	0.597613	23.1897
igneous	DK2_Z8_2	482.16	18.12	0.106	0.019	12.4	0.7	12.7		2.0	941	819	Matric		anhedral, hom rim			0.164557	21.53344	0.732759	1.925602	6.959459	9.591474	7.537688	38.88889	47.15447	56.77656	100.625	109.3117	167.7019	240.9024	1.324276	32.35772
igneous	DK2_Z10_2	466.12	29.62	0.071	0.042	13.4	1.1	7.8		2.0	891	773	Matric		anhedral, no o rim			0.021097	18.2708	0.786638	2.078775	4.256757	4.618117	18.09045	23.33333	17.47967	23.99267	31.25	28.34008	32.91925	58.53659	0.526261	3.235772
igneous	DK2_Z2_1	464.9	14.42	0.064	0.013	13.5	0.6	15.7		2.0	964	840	Matric		anhedral, hom rim			0.135021	55.13666	1.939655	5.317267	5.135135	9.776094	26.13065	34.72222	82.11382	137.3626	222.5	417.004	555.2174	723.5772	0.843341	27.69074
igneous	DK2_Z9_4	478.01	18.24	0.033	0.013	13.7	0.6	7.3		2.0	855	767	Matric		anhedral, no o core			0.011392	15.66069	0.974957	0.393873	2.364865	2.131439	11.55779	11.94444	41.70569	71.94444	267.875	449.2927	652.1739	987.4797	0.357764	23.1062
igneous	DK2_Z2_3	466.82	20.87	0.061	0.02	13.8	0.8	14.3		2.0	954	831	Matric		anhedral, hom rim			0.063291	47.14519	1.25	7.221007	11.28378	14.66483	22.11055	28.33333	47.15447	102.5641	129.375	206.4777	355.9006	577.2358	0.922101	26.1068
igneous	DK2_Z8_1	424.09	14.88	0.113	0.013	13.9	0.5	9.8		2.0	914	794	Matric		anhedral, no o rim			0.135021	22.3491	1.077586	6.345733	37.16216	19.89343	135.6784	263.8889	495.935	723.4432	1018.75	1445.344	2037.267	2170.732	0.280158	15.9991
igneous	DK2_Z2_4	461.89	19.6	0.044	0.017	14.0	0.7	19.7		2.0	990	864	Matric		anhedral, hom rim			0.135021	53.99674	3.265086	6.105033	17.56757	18.47247	31.15578	28.61111	17.47967	26.19048	37.5	37.65182	50.31056	39.02439	0.789587	1.252557
igneous	DK2_Z10_3	446.43	23.67	0.054	0.03	14.3	0.9	9.2		2.0	908	788	Matric		anhedral, no o rim			0.046414	16.63948	0.857328	1.466063	4.527027	12.26577	7.437186	17.22222	12.80163	32.23443	20.625	39.8664	45.34161	58.13008	2.112175	7.816139
igneous	DK2_Z8_3	411.52	26.7	0.098	0.051	14.7	1.4	10.6		2.0	922	801	Matric		anhedral, no o rim			0.050633	15.98395	0.465569	1.966064	7.689189	16.16341	15.57789	11.94444	32.52033	40.47619	33.75	51.417	45.58385	46.34146	1.563405	2.974823
igneous	DK2_Z10_1	422.65	11.18	0.046	0.01	15.2	1.5	10.4		2.0	920	800	Matric		anhedral, no o core			0.050633	18.10767	0.732759	0.459519	7.027027	2.309059	10.55276	34.44444	71.13821	172.1612	263.125	404.8583	565.2174	760.1626	0.268140	72.03446
igneous	DK2_Z9_1	422.3	14.34	0.04	0.011	15.4	0.8	9.2		2.0	908	788	Matric		anhedral, no o core			0.029536	20.55465	0.668103	2.460766	9.459459	2.841918	35.67839	97.5	186.1789	362.6374	510.625	753.0364	1037.267	1321.138	0.154696	37.02909
igneous	DK2_Z1_3	405.52	17.17	0.063	0.024	15.5	0.9	8.7		2.0	902	783	Matric		anhedral, no o rim			0.059072	19.73899	0.387931	1.750547	14.86486	8.880995	19.09548	16.38889	23.17073	11.35531	12.5	39.27126	6.21118	17.47967	0.527128	0.915383
igneous	DK2_Z1_4	398.25	15.66	0.057	0.023	15.7	0.9	6.4		2.0	872	755	Matric		anhedral, no o rim			0.035865	18.10767	0.344828	0.809628	2.635135	7.460036	15.57789	19.44444	17.88618	13.00366	18.125	16.59919	21.73913	7.317073	1.164554	0.469709
igneous	DK2_Z8_3	393.55	12.54	0.063	0.008	16.0	0.5	14.3		2.0	954	831	Matric		anhedral, hom rim			0.109705	33.27896	1.767241	5.908096	25.67568	10.30195	116.0804	222.2222	406.5041	677.6557	1000	1315.789	1819.876	2195.122	0.188703	18.91036
igneous	DK2_Z9_2	310.56	12.29	0.07	0.011	20.1	1.0	7		2.0	881	763	Garnet		anhedral, faint core			0.067511	13.02924	0.215517	0.83115	7.364865	5.861466	65.83333	119.2593	237.9675	369.5971	588.75	902.0248	1181.987	1453.658	0.242192	40.44715
igneous	DK2_Z8_2	301.75	10.47	0.051	0.006	21.2	0.8	8.8		2.0	903	784	Matric		anhedral, no o core			0.021097	18.43393	1.366534	7.221007	15.05757	7.460036	94.47236	213.8889	355.6911	608.0586	993.75	1214.575	1720.497	1979.675	0.197727	20.95507
igneous	DK2_Z9_2	294.64	8.91	0.052	0.008	21.7	0.7	6.1		2.0	867	751	Matric		anhedral, no o core			0.01308	19.90212	0.614224	5.47046	34.45946	14.03197	107.5377	277.7778	459.3496	798.5348	1156.25	1477.733	1950.311	2398.374	0.230507	22.30264
igneous	DK2_Z14_1	277.01	14.88	0.079	0.011	22.3	1.6	9.6		2.0	912	792	Matric		anhedral, no o core			0.046414	17.29201	0.528017	0.875274	10.81081	6.394316	23.11558	104.4444	186.5854	415.7509	481.25	817.8138	1080.745	1467.48	0.404494	63.48445
igneous	DK2_Z4_1	256

| | | |

| | | |

| | | |

| | | |

| | | |

| | | |

| | | |

| | | |

| | | |

| | | |

| | | |